Assessment of FUS-Tissue Interactions *In Vivo*

A DISSERTATION
SUBMITTED TO THE FACULTY OF THE GRADUATE SCHOOL
OF THE UNIVERSITY OF MINNESOTA
BY

Alyona V. Haritonova

IN PARTIAL FULFILLMENT OF THE REQUIREMENTS
FOR THE DEGREE OF
Doctor of Philosophy

Dr. Emad S. Ebbini, Adviser

July, 2015

Acknowledgements

My deepest gratitude goes out to my teacher, mentor, and biggest supporter – Emad Ebbini. Dr. Ebbini transformed me into the scientist I am today – strong, confident, and resilient. For that I will be eternally grateful. My heart followed the vision of Emad Ebbini starting from the very first day I joined his laboratory. Emad Ebbini inspired me to push the boundaries of ultrasound forward and never settle for less.

A big thanks goes out to Victor Barocas for recognizing the potential in me when we first met at a small coffee shop by St. Kate's. Victor was the first to recommend Emad Ebbini's laboratory for my PhD investigations. Many years later I owe much gratitude to Victor for guiding me down the right path.

My colleagues Dalong Liu, Andrew Casper, John Ballard and Mahdi Bayat were instrumental in my success in graduate school. Dalong, Andrew, John and Mahdi have answered a million questions and more, and have done it with great patience and kindness. I will always cherish their friendship.

Many thanks go out to Colleen Forster for her histological assistance in many of my projects. Colleen has worked tirelessly to help me capture and visualize the effects of focused ultrasound on tissue. Her innovative techniques and constant desire to learn made it an absolute pleasure to work together.

A special thanks to National Institutes of Health, International Cardio Corporation, and MnDRIVE Graduate Fellowship for funding me and my research.

My appreciation and love goes out to my mom and dad, Vladimir and Tatyana Haritonova, for being the rocks upon which I stand. They were a fountain of love and encouragement

throughout my PhD studies.

And finally, I want to thank the Hank Hohenstein for sitting with me on the bus when I was only 15 years old and painting a beautiful future ahead of me. Hank inspired me to dream beyond the imaginable and reach toward the sky. Hank and his wife, Susan, worked tirelessly to allow me to come to Minnesota and pursue an undergraduate degree. They have been a true blessing in my life. As I go forward, I will strive to make them proud every single living day.

Dedication

To my loving American Farther – Paba Hank. You made this journey possible. I could not have done this without you.

Love, Alyona

Abstract

Focused ultrasound (FUS) has been proposed for a variety of minimally invasive therapeutic applications, including tumor ablation, neuromodulation, targeted drug delivery and blood brain barrier opening. To date, FUS beams have been primarily monitored through MR and ultrasound diagnostic imaging modalities. The recent introduction of real-time dual-mode ultrasound array (DMUA) systems offers a new paradigm for the guidance of therapeutic focused ultrasound. The DMUA approach allows for inherent registration between the therapeutic and imaging coordinate systems.

In this thesis we investigated the use of ultrasound-based thermography to assess FUS-tissue interactions. Specifically, we focused on two aspects of image-guided therapy: 1) monitoring and localization of FUS-tissue interactions, and 2) tissue damage assessment. Towards this end, we presented first experimental results of ultrasound-guided transcranial FUS in a rat brain, both *ex vivo* and *in vivo*. DMUA imaging was used to monitor and localize FUS-tissue thermal interactions in real-time. The transcranial echo data allowed for a reliable estimation of temperature change in brain tissue, which had never been done before using ultrasound image guidance. Despite some measurable distortion and loss in focusing gain, transcranial FUS beams at 3.2 MHz were localized axially and laterally. This confirms the results obtained using DMUA-based transcranial ultrasound thermography. A high degree of focusing with the DMUA was then successfully leveraged to perform localized tissue damage assessment in both *ex vivo* and *in vivo*. The experimental results presented in this thesis demonstrate some of the unique aspects of image guidance using DMUAs, especially when FUS is subject to significant distortions as in transcranial applications.

Contents

List of Tables

List of Figures

Chapter 1

Introduction

1.1 Focused Ultrasound: Historical Overview

In the 1950s focused ultrasound (FUS) was extensively investigated by the Fry brothers at the Biophysical Research Laboratory, established at the University of Illinois. William and Francis Fry designed a complex system consisting of a multi-beam irradiator [1–3], allowing placement of trackless lesions measuring cubic millimeters in volume [4]. The custom-built system was used for a first comprehensive study on focused ultrasound effects in the central nervous system of *in vivo* animals [5]. The study revealed FUS ability to create reversible [5–7] and irreversible [1, 2, 5, 8] changes; the study also reported ultrasonic dosage curves for the brain as a function of intensity and time [5]. The Fry brothers supplemented their findings with a thorough histological examination, which revealed differential response of white matter compared to grey, in addition to preservation of blood vessels [5]. The extensive studies conducted *in vivo* brain structures in cats and monkeys [1–3, 5, 8], prepared the Fry brothers for a collaboration with Dr. Russell Meyers, Chief of Neurosurgery at the University of Iowa School of Medicine, to treat patients with Parkinsons disease [4]. Although successful results were demonstrated in nearly 50 patients [4], the widespread use of FUS therapy did not occur due to a seemingly better alternative medication – L-dopa [9]. Follow-up studies on a number of FUS-treated patients, 20+ years post treatment, revealed

no adverse effects in untargeted brain locations – confirming sparing of tissues located prefocally [4].

The remarkable results demonstrated by the Fry brothers, both in animals and human patients, were achieved without monitoring. The ability to target deep seated anatomical structures was possible through anatomical atlas referencing, where the skull was carefully placed inside the holder with ear bars, in addition to infra-orbital and oral clamps. Afterwards, the position was deduced by referring to a published anatomical atlas with coordinates. To achieve greater confidence in targeting, X-ray imaging was done to confirm internal landmarks [4]. Due to a lack of monitoring, much conjecture existed in the physical basis of ultrasound (US) effects on biological media.

Prior to the 1970s, the mechanism of FUS tissue destruction was largely attributed to mechanical effects of the beam [10]. In 1973, Lele and Pierce [11] emphasized the importance of heat generation during lesion formation process, as a result they proposed thermal hypothesis of the mechanism of ultrasonic focal destruction. The hypothesis found that for low acoustic power and short duration exposures, the diameter of the lesion was correlated to the temperature history at the lesion site [10]. Subsequently, a model was derived to predict cellular damage from the temporal temperature profile [10].

Lele also examined the role of cavitation during lesion formation in a fresh calf liver [10]. In this study a 2.7MHz source was used to generate 0.2 second and 0.3 second bursts of FUS. Monitoring was performed with a 50 μm thermocouple and a wide-band receiver, which recorded acoustic emissions during FUS bursts. The outcome of the study was identification of three distinct intensity regions, with unique heating and acoustic emission profiles: 1) intensity region < 500 W/cm^2 exhibited a predictable temperature rise without presence of acoustic emissions, 2) intensity region between 500 W/cm^2 and 1000 W/cm^2 revealed a higher than expected temperature rise and a subharmonic emission (stable cavitation), 3) intensity region > 1000 W/cm^2 displayed a dramatic increase in temperature and aharmonic emission (collapsed cavitation) in addition to subharmonic emission. These results demonstrate the first correlation between presence of cavitation and enhanced heating. The potential of controlled cavitation to facilitate a faster and a more effective FUS treatment was later proposed by Holt and Roy [12].

Monitoring of beam interaction with tissue led to important discoveries on focused ultrasound effects on biological media. Visualization of acoustic emissions with a wide-band receiver allowed Lele to identify intensity regions with unique acoustic signatures. The first two regions were deemed safe for FUS therapeutic applications, and the third region was pronounced unsafe, as collapsed cavitation could lead to uncontrollable internal hemorrhage and metastases [10]. Lele's work demonstrated that a thorough understanding of FUS effects on tissue was realized through monitoring of the FUS beam.

1.2 FUS Monitoring Modalities

MRI and ultrasound are currently the most widely used modalities for image guidance, both clinically and in research laboratories. These two methods are reviewed in [13]. Advantages of MR-guided focused ultrasound (MRIgFUS) include high soft tissue contrast, high spatial resolution, real-time temperature monitoring [14], and elastography monitoring [15]. The limitations of MRIgFUS monitoring are the high cost, and slow monitoring update rates on the order of 1 second [16].

Ultrasound, on the other hand, is less expensive, portable, and offers high-frame rate updates to the operator in the form of echogenicity changes on B-mode images [17, 18]. Additional ultrasound-guided focused ultrasound (USgFUS) capabilities, researched in the laboratory setting, offer highly localized quantitative tissue property maps in the form of temperature [19–23], elastography [24–28], vibroacoustography [29], and passive cavitation detection [10, 30, 31]. The major limitation of ultrasound is poor soft tissue contrast.

MRIgFUS and USgFUS systems use two separate modalities for FUS delivery and therapy monitoring. As a result, there are limitations on the therapeutic protocols imposed by the source of monitoring. For example, Sonavelle MR-HIFU system (Philips Healthcare, Helsinki, Finland) is limited by the slow temperature update rate (every 2.9 seconds) and a relatively poor temperature spatial resolution (2.5mm x 2.5mm) [32]. These limitations pose restrictions on the fibroid tumor size eligible for treatment [32]. They also result in long treatment procedures that can last more than 4 hours [32]. Ultrasound, unlike MRI, offers faster update rates, which are suitable for moving organs.

However, the form of feedback is limited to echogenic changes, which is indicative of boiling and/or cavitation presence and not purely thermal damage. There is a growing need for a dynamic monitoring modality, capable of motion compensation, obstacle visualization, and highly localized tissue property mapping.

1.3 DMUA: Brief Overview

At the beginning of this century a new paradigm was introduced to the field of focused ultrasound – Dual-Mode Ultrasound Array (DMUA). DMUA offers inherent registration of imaging and therapy planes, as it is uses the same elements for both purposes [33]. The common practice in the field had been to mechanically integrate a commercially available probe with the therapeutic transducer; prior to 1998 no one had attempted use of therapeutic arrays as a monitoring modality. Simon *et al.* [23] demonstrated use of DMUAs for monitoring applications in tissue-mimicking phantoms.

The design and construction of a therapeutic array emphasize the therapeutic efficacy of the prototype [33,34]. Characteristics of a therapeutic transducer are determined by the depth and the size of the acoustical window available [33]. To optimize heating rate at a specific depth, the array is designed with a relatively low operating frequency and the array (focusing) gain is maximized, resulting in a low f-number [33]. To achieve desired power at the target, the number of elements is minimized and efficiency is maximized, producing relatively large directive elements. These array characteristics – low operating frequency, low f-number, large directive elements – are common to therapeutic arrays. Unfortunately, they also introduce two limitations for imaging applications. First is a limited field of view, and second is a reduced dynamic range (observed if grating lobes are present due to very directive elements) [34]. Additional limitation, which had compromised imaging quality of therapeutic arrays, was rooted in material properties of the commonly used piezoceramic transducers. Piezoceramic transducers exhibited lateral cross-coupling between elements, which degraded imaging and therapeutic performance of the transducer. The cross-coupling problem was solved with the introduction of piezocomposite material [35]. An additional advantage of piezocomposite material is it allows fabrication of a highly concave transducer (low f-number) [35].

The difficulties associated with imaging by therapeutic transducers did not prevent the research community from demonstrating DMUA's major advantages. The first two advantages are high spatial resolution along with co-registration of imaging and therapy planes; both of these characteristics allow for imaging feedback with a high degree of sensitivity and specificity to the tissue changes at the focus. As a result, DMUA can be used for real-time monitoring of cavitation and/or boiling [33, 36] at the focus. Furthermore, DMUA offers a robust closed-loop control capable of addressing motion compensation [37] and tissue property-based adaptive lesion formation [38]. A third advantage of DMUA is the ability of DMUA to image interaction of the beam with the target region. This functionality is extremely valuable in the presence of obstacles (e.g. ribs), as was demonstrated in [39, 40] for treatment of liver cancer.

The intricacies of DMUA system and imaging modes will be further discussed in Chapter 2.

1.4 My Contributions

The main contribution of this dissertation is the assessment of FUS-tissue interactions using a DMUA with emphasis on thermal interactions. Detailed characterization of DMUA transcranial imaging was performed *ex vivo* in a Sprague Dawley rat, focusing on degradation of imaging resolution, loss of focusing gain, and ability to recognize anatomical landmarks. First, imaging performance was characterized through visualization of a wire target phantom, which captured point spread function of the array. Second, focusing gain was evaluated with a transcranial heating experiment and a thermocouple. Third, a comparative anatomy study was conducted to capture the same rat head with two modalities: DMUA and MRI.

The feasibility and safety of DMUA-guided brain therapies were demonstrated *in vivo* rodent model, where STF-based thermography provided feedback indicative of tissue interrogated with FUS in 8+ animals. An effort was made to further characterize temperature profiles observed *in vivo*, through careful assessment of DMUA focus distortions due to propagation through rat skulls (extracted from *in vivo* animals). The characterization study involved two complementary experiments. The first experiment

was designed to estimate the amount of energy transmitted through the rat skull and optimal transmission frequency. The experimental setup included two single-element transducers facing each other and a skull positioned in the middle. The second experiment enabled visualization of DMUA focus distortion through the skull at two different frequencies. DMUA focus mapping was done in axial-lateral and lateral-elevation profiles utilizing a hydrophone.

The DMUA's ability to interrogate tissue in a very small volume was demonstrated experimentally. This functionality could be extremely valuable for characterization of tissue before and after lesion formation. To evaluate tissue properties an interrogation shot, also known as a subtherapeutic shot, was delivered. The shot typically lasts 1 second or less and results in a temperature increase of a few degrees (1-3°C). There is no thermal damage resulting from subtherapeutic exposure, making it an ideal candidate for tissue probing. The temperature profile captured from the subtherapeutic shot was used to extract the initial heating rate (indicative of tissue absorption) from US thermography data collected before and after lesion formation *in vivo* rat. Further, computed thermography maps were registered atop lesions captured in gross photography. The merit of this method to access damaged tissue was also validated in a number of *ex vivo* bovine tissue samples.

1.5 Organization of This Thesis

Chapters in this thesis were organized as follows:

- Chapter 2 introduces the DMUA system, in addition to synthetic aperture and single transmit focus imaging, along with the algorithm for US-based thermography calculation.
- Chapter 3 provides characterization of transcranial synthetic aperture and STF-based thermography with DMUA.
- Chapter 4 discusses feasibility of guidance, monitoring and FUS delivery *in vivo* setting, in addition to *ex vivo* lesion formation.

- Chapter 5 characterizes DMUA focus through the skull, and aims to explain observations made in the previous chapter.
- Chapter 6 introduces quantitative parameter mapping based on ultrasound thermography data with a commercial US scanner both *ex vivo* and *in vivo*.
- Chapter 7 draws conclusions from the research findings and discusses future direction.

Chapter 2

DMUA System and Temperature Imaging

2.1 Image-guided Focused Ultrasound

The experiments presented in this thesis utilized either a DMUA integrated with a diagnostic ultrasound scanner or a full DMUA systems. Both systems are described in greater detail in this section.

2.1.1 Integrated Image Guidance Using DMUA and Diagnostic Ultrasound

Lesion formation and monitoring for the initial experiments was performed using a 3.5MHz DMUA integrated with a Sonix RP ultrasound (US) scanner (Ultrasonix, British Columbia, Canada). Figure 2.1(a) illustrates how the DMUA center opening accommodated HST15-8/20 probe connected to SonixRP. The HST15-8/20 probe had a 10 MHz center frequency and a 12 mm elevation focus. The characteristics of this probe resulted in an axially localized point spread function (axial resolution = 0.3 mm, lateral resolution = 2.4 mm) [36].

The DMUA utilizes a piezocomposite technology [41] and was manufactured by Imasonic

(Voray sur l'Ognon, France). The array had 64 elements, 1.3 mm in width X 6.8 mm in height, arranged in two rows on a spherical cross-section with a radius of 40 mm. The hole was positioned between two rows of elements and measured 16.5 mm in height. The inter-element spacing between each element was 0.2 mm. The element size is an important factor for the array, and will determine the therapeutic operating field. The therapeutic operating field is the region around the geometric focus where the focusing gain is within -3 dB of the maximum focusing gain at the DMUA geometric center. For the fenestrated DMUA the theraputic operating field extended ±5 mm axially and ±5 mm laterally from (x, z) = (0 mm, 40 mm).

The alignment of DMUA with HST15-8/20 enabled a co-axial registration between therapy and imaging plane, allowing for optimal visualization of tissue changes at the focus. As described in [42], the RF data acquisition from the Sonix RP and DMUA is performed at a high frame rate, allowing the tracking of tissue deformation in response to subtherapeutic HIFU beams. Subtherapeutic energy deposition raises the temperature only on the order of 1-3°C, resulting in no observable thermal damage at the focus. Monitoring tissue response to subtherapeutic FUS (at the lesion location) before and after lesion formation may provide a means of measuring quantitative changes in tissue property in response to tissue damage, e.g. tissue absorption and tissue diffusivity.

2.1.2 DMUA System

The majority of the experimental results presented in this thesis were collected with a full DMUA depicted in Figure 2.1(b). The array had 64 elements, 1.3mm in width X 14.5 mm in height, arranged in two rows on a spherical cross-section with a radius of 40 mm. The inter-element spacing between each element was 0.2 mm. The therapeutic operating field was defined at -3 dB and extended ±2.5 mm axially and ±3 mm laterally from the geometric center. During imaging and therapy applications DMUA was operated at 3.2 MHz. The control architecture for imaging and therapy was custom designed and is documented in greater detail by D. Liu and E. Ebbini [42] and Casper *et al.* [36].

The console depicted in Figure 2.2, illustrates the render interface available to the operator during imaging and therapy with a full 3.5MHz DMUA. The image (A) is an

(a) Fenestrated 3.5MHz DMUA

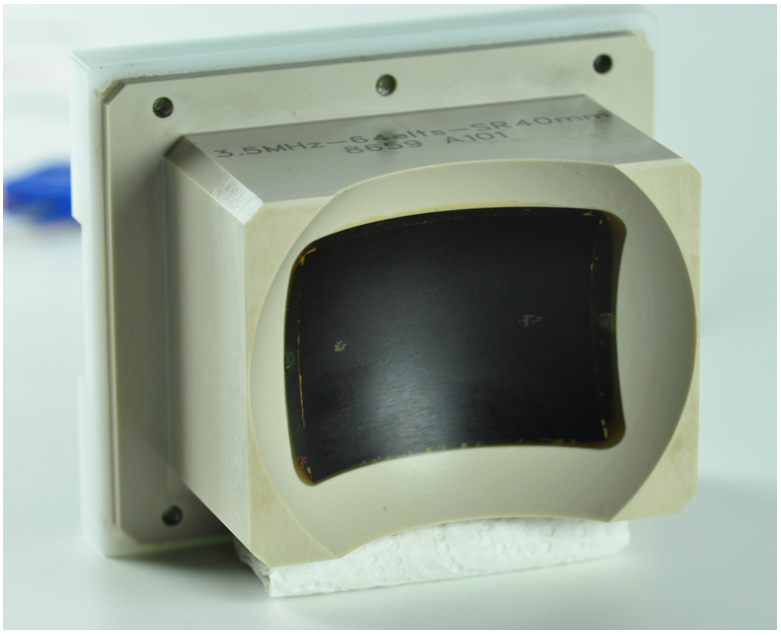

(b) Full 3.5MHz DMUA

Figure 2.1: Dual-Mode Ultrasound Arrays

SA image, with the temperature overlaid at a preselected region of interest (ROI). The imaging field of view (the region around the geometric focus where SA imaging produces spatially accurate, high-contrast maps of the object) extended ±10 mm and ±8 mm from the geometric center in the axial and lateral dimensions, respectively. Images (B), (C), and (D) represent axial-temporal, axial-lateral, and lateral-temporal cross-sections through the temperature profile. By examining each cross-section a localized heating spot is visualized at 40.5 mm axially and 2 mm laterally. Based on the temporal behaviour of the shot, pictured in (E), it is evident that the duration of the shot is 1 second long, with exponential heating response starting at 1 second and stopping at 2 seconds. The desktop console also allows the operator to define imaging and therapy parameters, for example imaging center frequency, focal depth, amplitude and duration of the desired exposure.

2.1.3 DMUA Imaging Modes

Synthetic Aperture Imaging

Synthetic aperture imaging is an imaging mode that synthesizes transmit and receive focus at every pixel in the image. This process results in a maximum sensitivity image. To form an SA image, a 32 element array would transmit 32 consecutive pulses and capture resulting echoes after each transmission. Both the full and fenestrated array had 64-elements, but upper and lower element rows were coupled, reducing the number of transmissions to 32. Equation 2.1 describes the image formation process for SA,

$$I(x_p, z_p) = \sum_{i=1}^{N_e} \sum_{j=1}^{N_e} A_i \cdot B_j \cdot s_{i,j} \left(\frac{R_{ip} + R_{jp}}{c} \right) \cdot D(\theta_i) \cdot D(\theta_j) \tag{2.1}$$

where N_e is the number of elements, A_i and B_i are the transmit and receive apodization weights, $s_{i,j}$ is the echo received on element j when transmitting with element i, R_{ip} and R_{jp} are respective distances from the transmit and receive elements to the image pixel P, $D(\theta_i)$ and $D(\theta_j)$ are the transmit and receive elements directivity weighting functions [33].

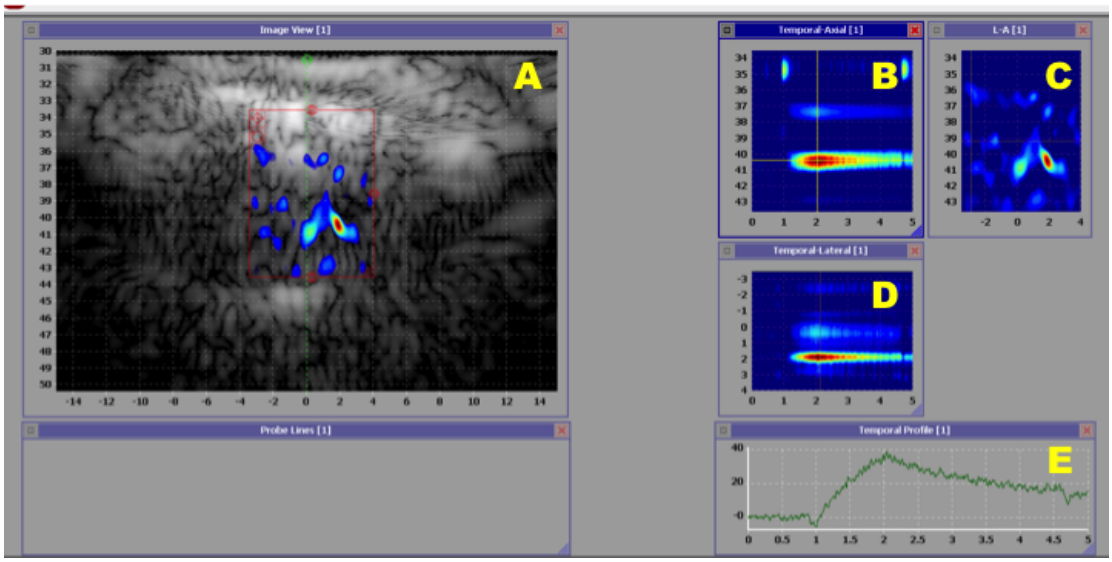

Figure 2.2: DMUA System User Console

According to equation 2.1, low resolution images reconstructed for every transmit-receive element combination were summed to form an SA image. The total number of images summed was 32 X 32 = 1024. As a result of this summation process, the resolution and SNR were significantly improved. To further improve image quality the directivity matrix was incorporated, it suppressed signal from low SNR regions and suppressed grating lobes due to coarse aperture sampling [33,34]. The directivity weighting function is described by the equation 2.2,

$$D(\theta) = \frac{\sin[kd\sin(\theta)/2]}{kd\sin(\theta)/2} \tag{2.2}$$

where $k = 2\pi/\lambda$, d is element width, and θ is an angle between vector from element to geometric center and vector from element to pixel P [33].

Synthetic aperture imaging mode was utilized extensively throughout this thesis. An example of an SA image of a 50 μm wire at the focus is depicted in Figure 2.3(a). The wire is localized at (x,z) = (0mm, 40mm) and appears more elongated in the axial dimension, which is consistent with the point spread function of the array. Currently, the DMUA system designed in our laboratory allows simultaneous therapy and SA monitoring at a frame rate of $\approx$ 30fps. During *in vivo* experiments SA imaging allowed to localize therapeutic plane through the skull of the rat, enabling visualization of skull cross-section and cheek muscles. SA imaging was also used to inspect lesions for presence of cavitation and/or boiling [33].

Single-Transmit Focus Imaging

Single-transmit focus imaging is an imaging mode, where a focused transmit beam is used to form a 2D image. To form an STF image a 32-element array would transmit a single focused wave on all of the elements and capture the resulting echoes. Equation 2.3 describes the STF image formation process:

$$I(x_p, z_p) = \sum_{j=1}^{N_e} B_j \cdot s_j \left(\frac{R_0 + R_{jp}}{c} \right) \tag{2.3}$$

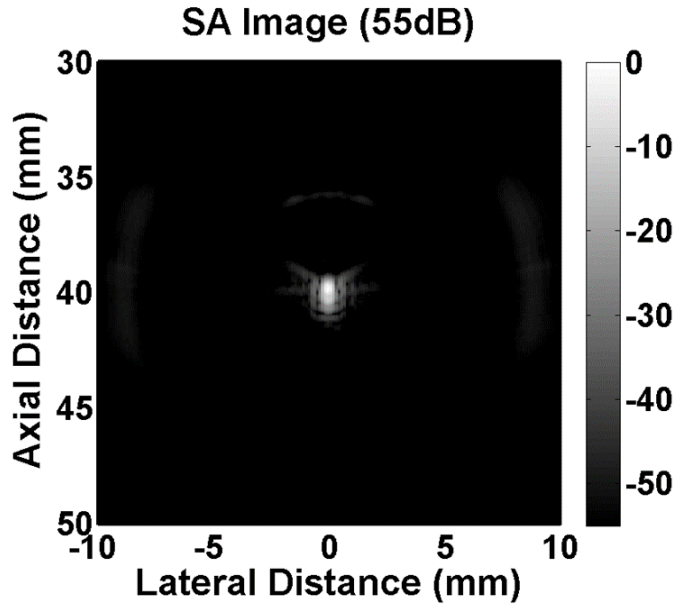

(a) Synthetic Aperture Image

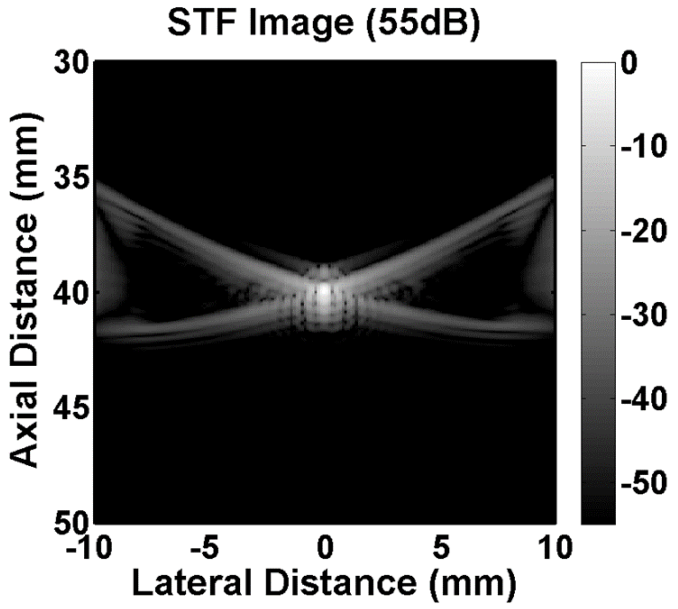

(b) ingle-Transmit Focus Image

Figure 2.3: Exaples of an SA and STF images

where $s_j(t)$ is the echo received on element j due to the tramsmitted beam and R_0 is a fixed distance to the focus of the transmit beam. The rest of the variables are similar to those presented for the SA image formation [33].

Equation 2.3 is a simplified version of the equation 2.1, depicting only one sum. This resulted due to the change in the transmit sequence. As a result of this change, there arose two advantages for imaging with STF. First advantage is the ability to visualize obstacles on the path of the beam. A successful STF-based refocusing was demonstrated in the presence of Plexiglas ribs [40]. This application has the potential to enable a more robust liver ablation therapy around the ribs [40]. The second advantage of STF imaging is the speed of feedback, which can easily reach 1000 frames/second. Fast update rates allows for real-time monitoring during ablation procedures, allowing operator to visualize tissue-specific changes and tissue motion on the order of milliseconds [36]. The main disadvantage of STF imaging is its limited lateral resolution. An example of STF image of a 50 μm wire is depicted in Figure 2.3(b). The wire is located at (x,z) = (0mm, 40mm), however it is no longer localized in the lateral dimension.

Spatial Resolution

Two methods were used to estimate spatial resolution of the imaging modality. The first method is based on imaging through a cross-section of a wire phantom, as seen in Figure 2.3(a). Axial and lateral traces are then plotted through the maxima of the wire, and resolution values are estimated based on a 6-dB cutoff. The second method is derived from a uniform region of the target. To estimate axial and lateral resolution, a correlation based approach was used. Equations 2.4 and 2.5 describe computation of the axial (S_{cx}) and lateral (S_{cz}) cell size:

$$S_{cx} = \int_{X}^{-X} \frac{C_I(x,0)}{C_I(0,0)} dx \qquad (2.4) \qquad\qquad S_{cz} = \int_{Z}^{-Z} \frac{C_I(0,z)}{C_I(0,0)} dx \qquad (2.5)$$

where C_I(x,z) is a 2D autocovariance function.

2.2 Ultrasound Thermography

In the mid-1990's two research groups, Seip *et al.* [19,20,43] and Moreno *et al.* [21,22,44], independently proposed a noninvasive method for monitoring temperature during FUS treatments. The proposed method relied on two, temperature dependent, phenomena: speed of sound and tissue expansion [20,44]. The first variable, speed of sound, increases linearly with temperature during small changes in temperature ($< 10°C$) [22, 45, 46]. The second variable, tissue expansion, also exhibits a liner change in the presence of highly focused ultrasound beam [20, 44]. The change in the speed of sound result in an apparent shift in the RF-data; the change in tissue expansion lead to a physical shift of the RF-data. Thus, in order to estimate temperature, echo shifts are computed first.

2.2.1 Displacement Computation

To compute echo shifts between two consecutive frames a 2D complex autocorrelation method was used, previously described by Simon *et al.* [23]. During the computation two dimensions were considered, axial (z) and lateral (x). There are four key steps involved in estimation of the incremental time time-shift. The first step, described by equation 2.6, computes convolution between discrete-time sampled RF-echo data, r(m,n,s) and an FIR Hilbert Transform, h(m):

$$\breve{r}(m,n,s) = r(m,n,s) * h(m) \tag{2.6}$$

The second step is to compute analytic signal, as seen in equation 2.7:

$$\hat{r}(m,n,s) = r(m,n,s) - j\breve{r}(m,n,s) \tag{2.7}$$

The fourth step computes the q-th lag along the axial dimension, where an observation window M X N is chosen in the axial and lateral dimensions respectively,

$$\hat{\gamma}(m,n,;q,0) = \sum_{m'=-\frac{M}{2}}^{\frac{M}{2}-1} \sum_{n'=-\frac{N}{2}}^{\frac{N}{2}-1} \hat{r}(m+m',n+n',s-1)\cdot\hat{r}^{*}(m+m'+q,n+n',s-1) \quad (2.8)$$

where * represents complex conjugation.

The final step is to compute incremental time-shifts from the phase of the autocorrelation function at lags q=-1, q=0 and q=1 according to the equation:

$$\delta\hat{t}(m,n) = \frac{2\angle\hat{\gamma}(m,n,;0,0)}{\angle\hat{\gamma}(m,n,;1,0) - \angle\hat{\gamma}(m,n,;-1,0)} t_{sp} \quad (2.9)$$

where $\angle$ is the angle symbol. For a more thorough discussion of the algorithm please refer to [23].

2.2.2 Temperature Computation

After infinitesimal displacement was computed, temperature was estimated according to a recently proposed differentiator-integrator filter by Bayat *et al.* [37]. Equation 2.10 illustrates an IIR filter which performed recursive differentiation and integration of the echo shifts.

$$\breve{\triangle}\theta = \frac{-2}{\alpha\tau + T_s(\alpha+\beta)} \frac{1-z^{-1}}{1-\frac{\alpha\tau - T_s(\alpha+\beta)}{\alpha\tau + T_s(\alpha+\beta)} z^{-1}} \breve{\delta}\tau \quad (2.10)$$

where $\breve{\triangle}\theta$ and $\breve{\delta}\tau$ are z transforms of $\triangle\theta$ and $\delta\tau$, T_s is sampling time of the RF-data, α is linear coefficient of thermal expansion, β represents thermal dependence of speed of sound in tissue, and τ=$2z_0/c$.

The model upon which the filter was derived builds upon Simons *et al.* [23] paper. Major differences in the new derivation are: 1) accounting for non-uniform baseline temperature; and 2) reduction of spatial temperature variations as well as artifacts.

Figure 2.4(a) depicts an axial-temporal temperature profile through the center of the DMUA focus. In the figure positive and negative temperatures are alternating, starting

from 35mm and extending to ≈ 41 mm. Two most prominent heating locations were present at (z) = 38.8 mm and (z) = 40.1 mm, their representative temporal curves are visualized in Figure 2.4(c). The temporal response for both locations revealed almost identical exponential heating and decay profiles with the exception of a negative sign. In 1998 Simon *et al.* suggested use of a threshold-based approach to eliminate negative temperatures, where only positive temperatures were displayed. Temperature profiles presented in this thesis follow threshold-based approach, and display temperatures only above 0∘C as seen in Figure 2.4(b).

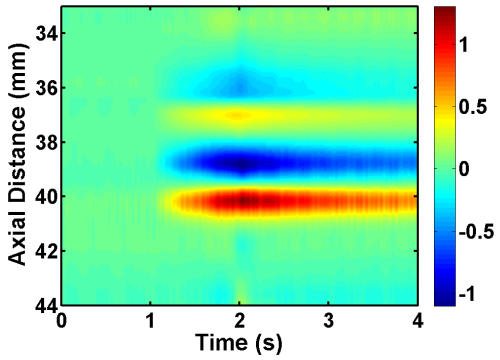

(a) Temperature (Positive & Negative)

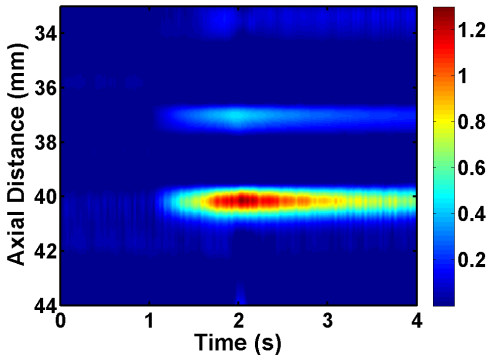

(b) Temperature (Negative)

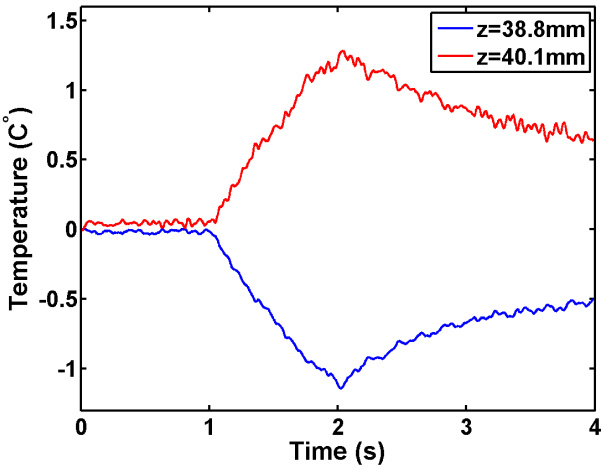

(c) Temperature Traces

Figure 2.4: STF-based Thermography

Chapter 3

Characterization of Transcranial Imaging with DMUA

3.1 Introduction

The dual-mode ultrasound array (DMUA) is a new paradigm in the field of focused ultrasound, offering the user full capabilities of a standalone therapeutic platform. We have designed and begun an experimental validation study of a DMUA system for forming, monitoring, and characterizing subtherapeutic pulsed transcranial focused ultrasound (tFUS) fields in an *ex vivo* rat model. In this chapter, we present *ex vivo* results that demonstrate the capabilities of a DMUA to place image-guided tFUS beams as well as monitor their interactions with brain tissue. The results shown provide experimental validation of the ability of DMUA imaging to capture important landmarks to allow the targeting of specific regions within the brain. In addition, we present experimental results demonstrating the effectiveness of DMUA-based, real-time transcranial ultrasound thermography (UST) to monitor and localize the thermal response to subtherapeutic applications of tFUS. The UST estimates were validated using thermocouple measurements in *ex vivo* experiments.

3.2 Methods

3.2.1 DMUA System

The 3.5 MHz DMUA described in Section 2.1 was used to perform transcranial therapy imaging and therapy in the rat model. The DMUA was operated in two imaging modes: synthetic aperture (SA) and single transmit focus imaging (STF). SA imaging was used for the guidance of transcranial focused ultrasound (tFUS) treatment. STF imaging was used to calculate thermography estimates and monitor the lesion formation process. Both SA and STF images were beamformed with the speed of sound at 1520 m/s. The results are detailed in this chapter.

Calibration of Subtherapeutic FUS Output

As the thermal effects of ultrasound are largely dependent on acoustic power, an ultrasound power meter was used to calibrate the acoustic output of the DMUA. To determine how various driving voltages correlated to acoustic output, individual subtherapy exposures were calibrated with an ultrasound power meter (Ohmic Instruments, Easton, MD, USA). Consequently, a subset of subtherapeutic exposures was identified: 0.25, 0.56, 1.0, 1.26, 2.25, 4.0, 6.25, and 9 Watts (acoustic). Acoustic power can be further translated into focal intensity by taking into account the gain of the array and its surface area (11.46 cm^2). Final FUS focal intensities ranged from 100 W/cm^2 for the 0.25 W exposure to 3500 W/cm^2 for the 9W exposure.

3.2.2 Visualization of Anatomical Landmarks with the DMUA

To guide transcranial treatment with the DMUA, it was necessary to identify anatomical features on the SA images. The characterization of anatomical features involved imaging the head from a sacrificed rat with two modalities: ultrasound (DMUA) and MRI. A 3D volume of SA images was acquired by moving a 3D servomotor stage in 1 mm increments, spanning 21 mm in length starting at the eyes and moving towards the ears of the rat. The MRI volume was acquired with a 9.4 Tesla scanner and a quadrature

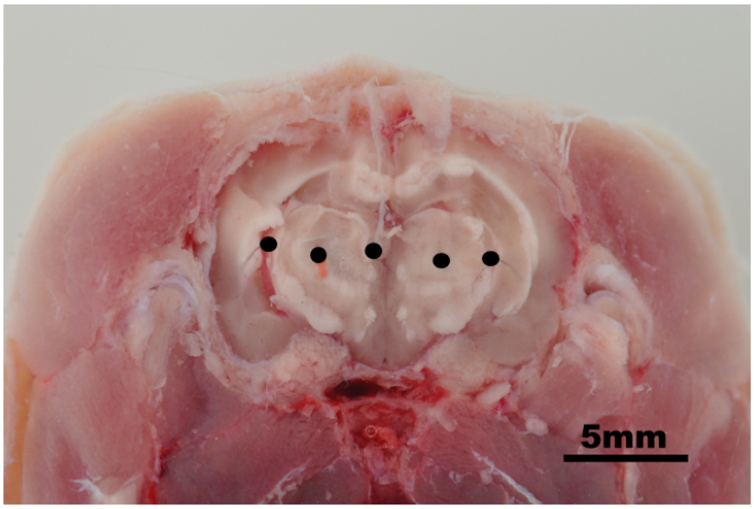

(a) Five wires inserted in the brain tissue

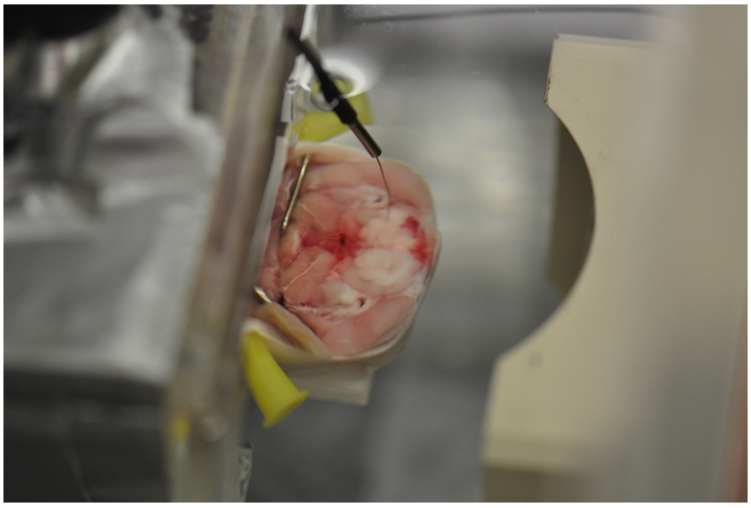

(b) Brain positioned in front of DMUA

Figure 3.1: Experimental setup for determination of spatial resolution with SA imaging.

coil. The voxel resolution of the collected MRI images measured 117 μm $\times$ 117 μm $\times$ 234 μm in the axial, lateral, and elevation dimensions, respectively.

3.2.3 Spatial Resolution of Synthetic Aperture DMUA Imaging

To characterize the imaging resolution of the synthetic aperture imaging through the skull, a wire resolution test was performed. In preparation for wire insertion, the skull was transected with a bone saw (Mar-Med Inc., Cleveland, OH, USA) through the coronal plane at two locations, caudal with respect to the eyes and rostral with respect to the ears, isolating the middle of the brain. Transecting the skull allowed easy access to the brain for the insertion of five 50 μm wires. As seen in Figure 3.1(a), five individual wires were carefully inserted with the help of forceps. Afterwards, the skull was secured to a rubber holder and positioned for imaging with the DMUA, as seen in Figure 3.1(b). To estimate the lateral and axial resolution, all five wires were individually aligned with the geometric center of the array (x, z) = (0, 40)mm. The lateral and axial traces through the wire centers were subsequently examined and resolution values were computed based on a -6dB cutoff criterion.

3.2.4 Power Calibration with a Thermocouple

To further calibrate power exposure, we collected thermocouple (T/C) measurements for a subset of subtherapeutic and therapeutic exposures. A 200 μm T-type copper-constantan thermocouple (Omega, Stamford, CT) was inserted in the brain, as seen in Figure 3.1(b). The shaft of the thermocouple was perpendicular to the imaging plane, which allowed for a direct visualization of the T/C cross-section on the SA image. Using transcranial FUS and a 3D servomotor stage, the thermocouple junction was localized, and two subsequent tests were performed:

1. *Profiling the tFUS Beam*: Six 1-second tFUS shots were generated at the geometric center (x, z) = (0, 40)mm. The shots were delivered with the T/C and the brain at six different locations around the intended focus (200 μm between locations). This test measured how sharply the heating rate dropped in the vicinity of the target point (in both axial and lateral dimensions).

2. *Bracketing the tFUS Heating Rate*: The T/C was positioned in the vicinity of the tFUS focal spot to minimize the viscous heating while maintaining the sensitivity to the local heating. A 1-second exposure was conducted for five different power settings at the same focal location. STF imaging frames were collected synchronously with T/C measurements for each shot. Ultrasound thermography was used to estimate the temperature change at the expected tFUS focal spot for each exposure. This test served to compare the sensitivity of DMUA-based UST to thermocouple measurements as well as providing a calibration for expected temperature rise during planned *in vivo* experiments where T/C measurements could not be used.

3.2.5 Transskull Lesion Formation *Ex Vivo*

Focused ultrasound therapy was delivered in sacrificed normal rats with no prior FUS treatment. After the sacrifice, the head of the animal was separated from the body and secured to a motorized stage, similar to the setup depicted in Figure 3.1(b) except the skull was not transected with a saw. Using SA imaging guidance the therapeutic FUS lesions were placed 6-8 mm below the skin in the left hemisphere of the animal brain. The right hemisphere of the brain served as a control upon histological examination.

There were a total of three varying exposure levels and time durations: 36 W for 1 second, 49 W for 1 second and 64 W for 0.6 seconds (respective power values were extrapolated from subtherapeutic doses; skull attenuation was not taken into account). For each exposure and time combination three shots were conducted, resulting in a total of nine insonications. During the lesion formation procedure, monitoring was performed with STF imaging (with the imaging plane parallel to the coronal plane) and was carried out before, during and after shot delivery with a frame rate of 400 fps.

Upon completion of the experiment, the brain was extracted, formalin-fixed and paraffin embedded. A histotechnologist obtained axial sections through the animal brain at 300 μm intervals. The axial plane of the animal brain coincided with the elevation plane of the transducer. Sectioned cross-sections were stained with hematoxylin and eosin stain and submitted for detailed examination by a certified neuropathologist.

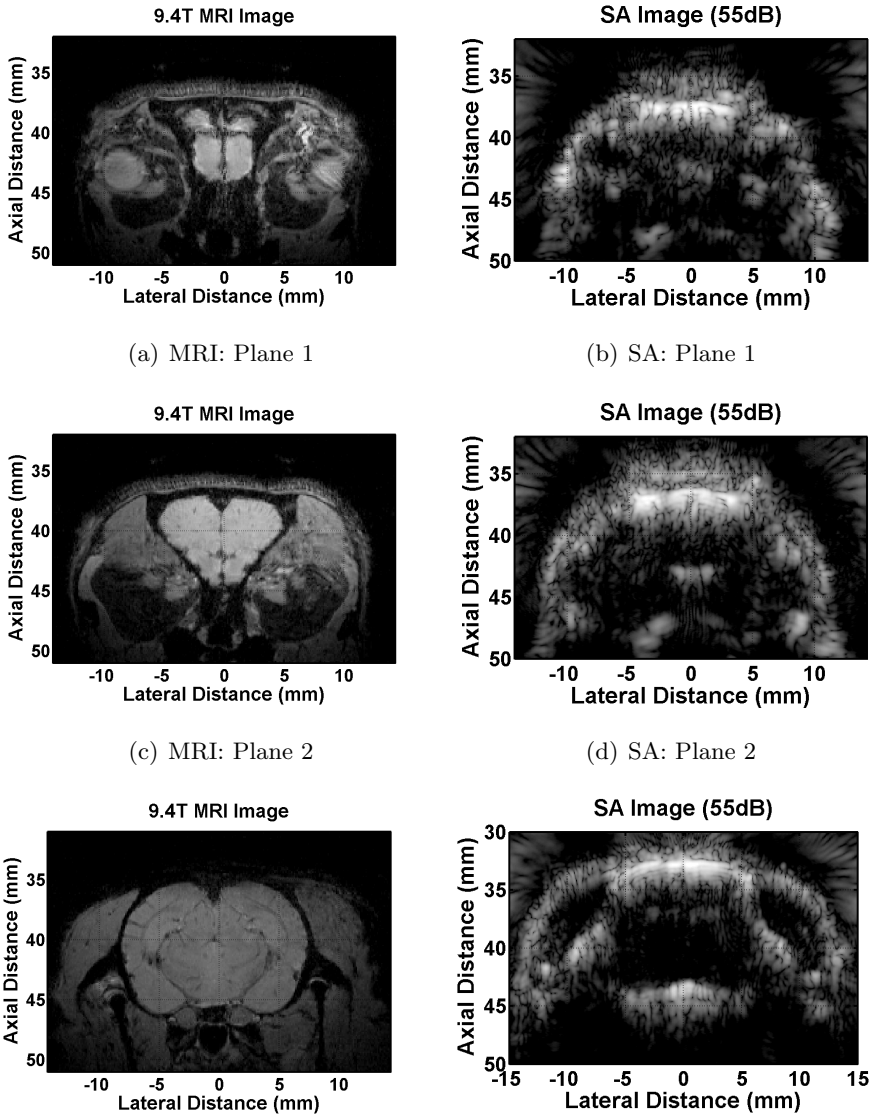

(a) MRI: Plane 1

(b) SA: Plane 1

(c) MRI: Plane 2

(d) SA: Plane 2

(e) MRI: Plane 3

(f) SA: Plane 3

Figure 3.2: MRI and SA (55 dB) cross-sections of three representative planes.

3.3 Results

3.3.1 Anatomical Correspondences: MRI and DMUA

Figure 3.2 shows MRI (left) and SA (right) images from the same animal. The comparison revealed several anatomical landmarks on the MRI scan that were also apparent in the SA images. The dorsal aspect of the skull was clearly visualized, capturing the frontal, parietal, interparietal and occipital bones. The floor of the cranial cavity and cheek muscles shown in the MRI were also clearly outlined in the SA images. Identifying anatomical landmarks through feature visualization on registered MRI and SA images, supports the use of DMUA as a therapy guidance modality for small rodents.

3.3.2 Spatial Resolution of Synthetic Aperture DMUA Imaging

A synthetic aperture image containing five 50 μm wires is depicted in Figure 3.3(a). Five individual SA acquisitions were used to produce this c-scan image, and with each capture the geometric focus was closely aligned with the location of a wire. The lateral axis on the image was aligned with the middle wire, located at 0 mm and the outermost wire segments located at -5 mm and 5 mm. In the axial dimension the echoes for all wires were located at $\approx$40 mm. The fourth wire from the left has a unique echo, which can be attributed to a slight bend introduced upon its insertion.

Axial and lateral traces through the middle wire are also seen in Figure 3.3(b) and Figure 3.3(c), respectively. When examining the axial profile of the middle wire, the reflection from the skull appears first at about $\approx$32 mm and its amplitude was set to 0 dB, and the wire was localized at 40 mm axially and -10 dB in amplitude. In the lateral profile, Figure 3.3(c), the wire presented a peak at 0 mm. The resolution values were evaluated at -6 dB and correspond to 440 μm and 560 μm in the axial and lateral dimensions respectively. Similar values were computed for each inserted wire, and are summarized in Table 3.1.

The summarized results give further evidence that DMUA has the ability to visualize structures through the brain with sub-mm accuracy in the lateral and axial dimensions.

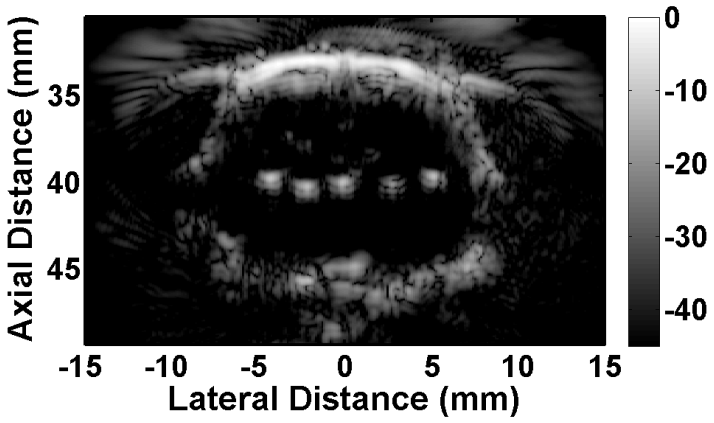

(a) Synthetic-aperture image of brain cross-section

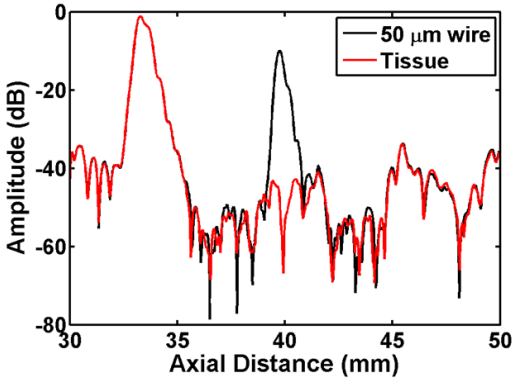

(b) Axial trace through the center wire

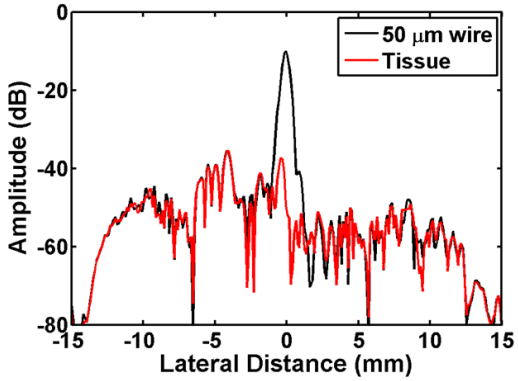

(c) Lateral trace through the center wire

Figure 3.3: Results of transcranial PSF measurement.

The wire echoes appeared minimally distorted through the bone and are in close agreement with estimates obtained in a water setting. The variation in the resolution values for each individual wire segment can be explained by their varying position within the skull.

Table 3.1: Spatial Resolution of a 50 μm Wire Embedded within Brain Tissue

Resolution	**L1**	**L2**	**L3**	**L4**	**L5**
Axial (μm)	440	510	480	340	440
Lateral (μm)	560	640	553	462	495

3.3.3 Characterization of the Transcranial FUS Heating Focus and the Calibration of DMUA Thermography

To characterize DMUA focal heating, a T/C was inserted perpendicular to the imaging beam of the array. With the guidance of synthetic aperture imaging, the tip of the T/C was visualized in Figure 3.4(a). Colored dots depicted in the figure represent six targeted locations, spaced 0.2 mm apart, where an FUS shot was delivered with a power of 4 W and exposure of 1 second. Temperatures recorded at each of the locations were plotted in Figure 3.4(b). The temperature curves revealed a sharp drop in temperature outside of a narrow lateral band, as seen in the orange and yellow lines. Temperatures recorded along the axial dimension exhibited a less pronounced change in the heating rate, due to the longer beam length along the axial axis. The dark blue dot was observed to have the largest increase in temperature, indicating it was the closest to the T/C junction.

After calibrating the DMUA spatially, the acoustic power of the DMUA was calibrated in relation to the temperature change in the T/C at one location. The location closest to the T/C junction, represented by the blue dot, was chosen during this calibration step. At this location five subtherapeutic shots (0.25 W, 1 W, 2.25 W, 4 W, and 6.25 W) were delivered with duration of 1 second.

Figure 3.4(c) shows the T/C temperature before, during and after exposure for each shot. Figure 3.4(d) shows the change in temperature occurring with each shot based on

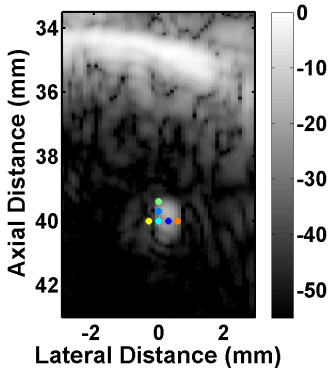

(a) Six spatial heating locations close to the thermocouple.

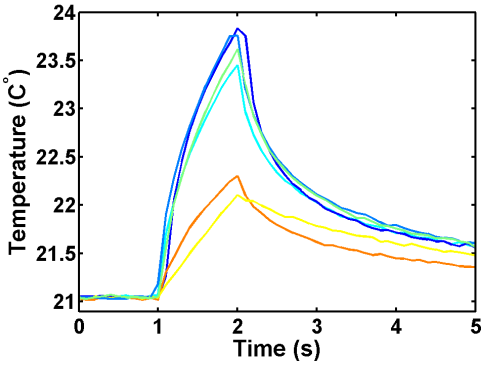

(b) Thermocouple temperature for locations in (a).

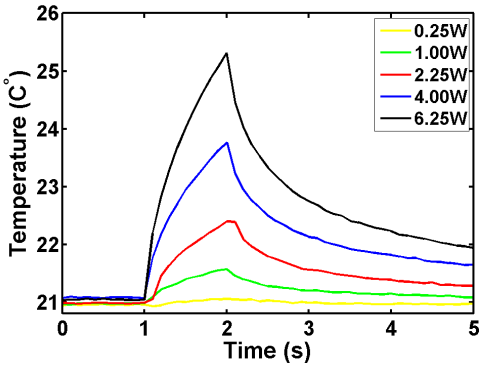

(c) Thermocouple temperature

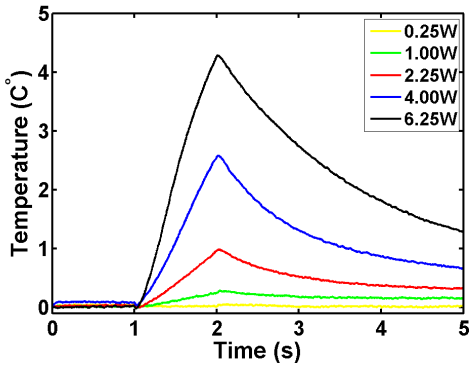

(d) STF-based UST

Figure 3.4: DMUA tFUS subtherapy with thermocouple calibration: (a) Six spatial heating locations around the thermocouple junction (0.2 mm spacing), (b) recorded temperatures for the six locations seen in (a), (c) STF-based UST and (d) thermocouple measurements recorded at the dark blue dot in (a). Legends are representative of ultrasound power levels in water measured in Watts.

the STF thermography, with the ΔT axis set to match the amplitude of thermocouple estimates. The major difference between the temperatures acquired through the T/C and those acquired through STF thermography was that for the thermocouple measurements, during the FUS ON phase, the temperature curves approximated an exponential change function and for the STF thermography the curves resembled a linear function. In contrast, during the cooling phase both T/C and STF thermography revealed exponential decay functions. This effect was most likely due to the close proximity of the T/C to the tracking region, thus introducing an artifact. The exponential rise of the temperatures was more pronounced when the T/C was removed.

3.3.4 Transskull Lesion Formation *Ex Vivo*

Figure 3.5(a) shows an example of a lesion formed in the left hemisphere with a 1 second tFUS exposure at an acoustic power of 49 W (power was linearly extrapolated based on low power measurements; nonlinear wave interaction was not taken into account). The cells were thermally coagulated, and a sharp transition was observed between coagulated and normal tissue. A more detailed depiction of the lesion is seen in Figure 3.5(b), where the perimeter of the lesion was outlined with a red marker. The diameter of the lesion cross-section was measured at 689 μm. The lesion was visualized in two axial histological slices, thus the height of the lesion was between 600 μm and 900 μm. The control region captured in Figure 3.5(c) did not reveal presence of coagulated or compromised cells.

Additional shots were conducted, but only one lesion was observed on the histology. This one documented result demonstrates the high degree of transcranial focusing possible with the DMUA beam.

3.3.5 Conclusion

The feasibility of real-time image-guided placement and monitoring of tFUS beams using dual-mode ultrasound arrays was demonstrated in an *ex vivo* rat model. Synthetic aperture DMUA imaging was shown to reliably capture key anatomical features delineating the scalp, the skull and the base of the skull. Subtherapeutic lesion formation

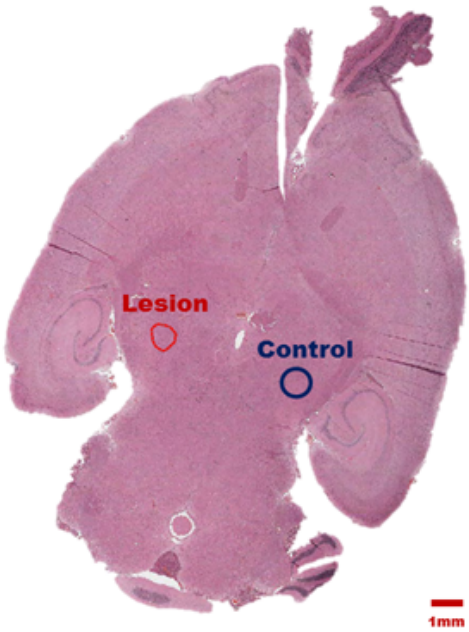

(a) Full Section (0.4X)

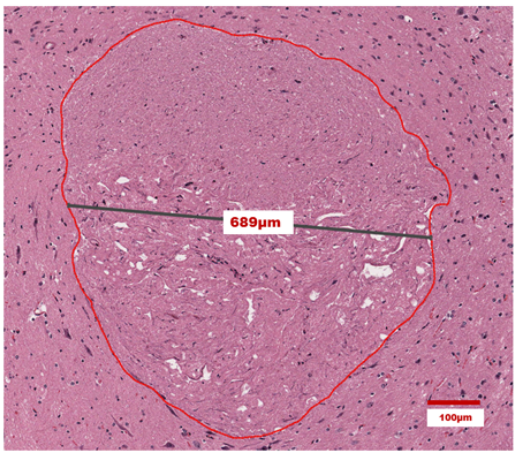

(b) Lesion (10X)

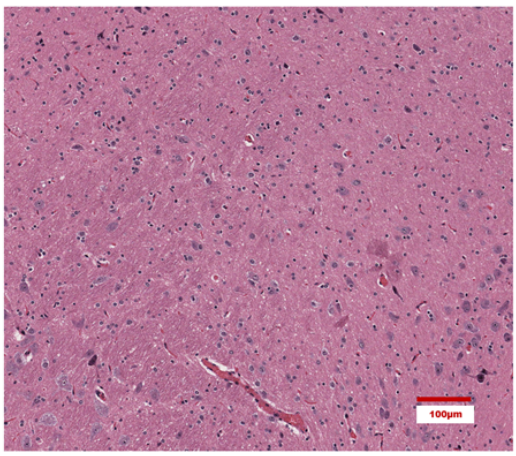

(c) Control (10X)

Figure 3.5: Thermal lesion formed in the left hemisphere of the rat brain.

with DMUA in the vicinity of a thermocouple validated the high degree of spatial focusing possible with the DMUA. These findings were further validated during histological examination of the DMUA formed lesions. The next chapter will build upon these *ex vivo* results, and demonstrate real-time image-guided placement and monitoring of subtherapeutic and therapeutic tFUS.

Chapter 4

In Vivo Real-Time Transcranial Therapy and *Ex Vivo* Lesion Formation with DMUA

4.1 Introduction

Building on the *ex vivo* work from Chapter 3, the experiments in this chapter demonstrated the capabilities of a DMUA to deliver and monitor subtherapeutic and therapeutic tFUS. First, subtherapeutic tFUS monitoring was tested in eight animals in the presence of breathing and pulsation. After three days the animals were sacrificed and the tissue was evaluated by a neuropathologist. Second, therapeutic tFUS was performed *ex vivo* and tissue changes were monitored with the DMUA.

4.2 Methods

The *in vivo* therapy and monitoring was performed with a full 3.5 MHz DMUA system. To establish a successful coupling of the DMUA to the head of the animal, the DMUA was encapsulated inside a water bolus as seen in Figure 4.1(a), and a layer of ultrasound

gel was applied to the surface of the bolus. The *in vivo* experiments in eight Sprague Dawley rats were performed under the IACUC protocol (ID # 1403122A).

4.2.1 Temperature Imaging with DMUA (*In Vivo)*

At the start of the procedure, the animals were given an intramuscular injection of 9-10 mg of Ketamine and 1 mg per 275-299 g of body weight of Xylazine. After the anaesthesia took effect, the head of the animal was shaved with Oster clippers (Philips, Amsterdam, Netherlands); to remove remaining fine hair a thin layer of a depilatory cream (Church & Dwight, Ewing, NJ, USA) was applied to the head.

For the remainder of the experiment the rats were anaesthetised with a Harvard Apparatus (Harvard Apparatus, Holliston, MA, USA), which delivered a constant flow of isoflourane and oxygen. Also, to ensure minimal movement of the head and minimize the effects of breathing, the head was secured in a stereotaxic frame (World Precision Instruments, Inc, Sarasota, FL, USA). Throughout the procedure a veterinary technician was responsible for monitoring the well-being of the animal, including breathing rate and body temperature. For four out of eight animals, vital signs (ECG and body temperature) were continuously monitored with a BIOPAC system (BIOPAC Systems, Inc., California, USA).

The DMUA procedure started with identifying a location within the skull under the guidance of synthetic aperture imaging. To ensure that the focal point of the transducer was at least 5 mm under the skin surface, the cranium ceiling was positioned at 34+/-2 mm and the cranium floor at 45+/-2 mm in the axial dimension.

During FUS delivery, locations of interest were identified under SA guidance. To minimize movement, the array beam was often steered +/-2 mm in axial and lateral dimensions. When axial adjustment of the therapeutic operating field was needed, the bolus was either inflated or deflated to deposit energy at the desired location.

As in previous *ex vivo* experiments, the first step was to bracket energy delivery to five (0.25 W, 1.00 W, 2.25 W, 4.00 W, and 6.25 W) subtherapeutic levels, and identify the lowest level sufficient to visualize the temperature rise above the noise floor. Subsequent

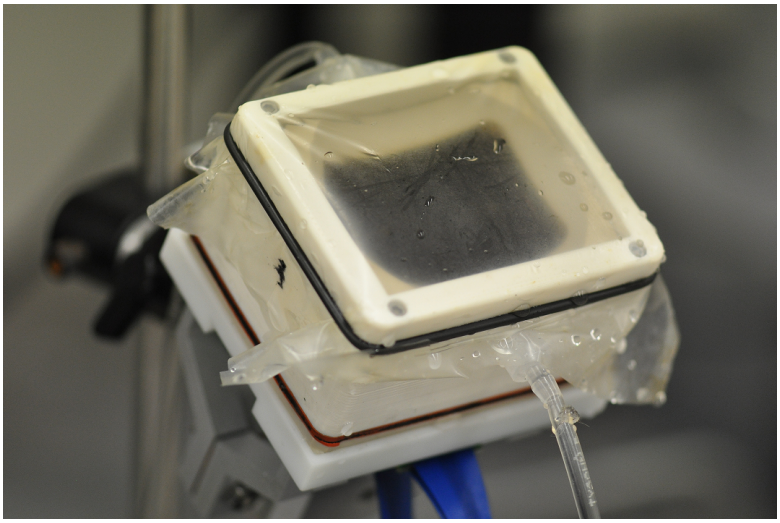

(a) DMUA encapsulated inside a water bolus.

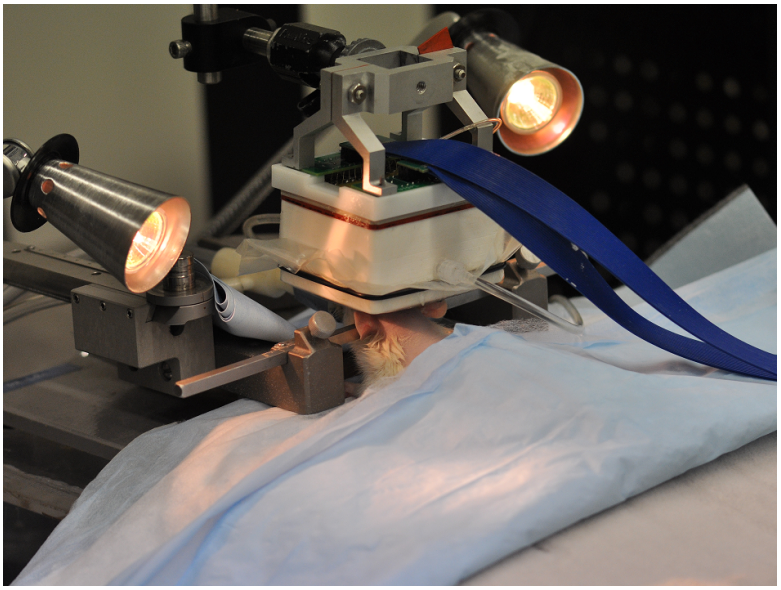

(b) Rat fixed in stereotaxic U-frame for transcranial imaging with DMUA.

Figure 4.1: Transcranial DMUA imaging and subtherapeutic heating *in vivo*.

exposures were delivered at the pre-determined power level. The exposure duration was kept constant for all experimental subjects at 1 second. A total of 38 locations were interrogated with 2 minutes between shots in eight animals; in 66% of the interrogated locations the FUS shot was delivered at least twice to test the repeatability of the temperature measurement.

Histological Evaluation

The animals survived for a period of three days under the watchful observation of veterinary technicians and a veterinary physician. The sacrifice was performed with approximately 5 minutes of CO_2 asphyxiation. Afterwards, in the first three animals the tissue was immediately excised, fixed in formalin and processed. A histotechnologist obtained hematoxylin and eosin stained sections at intervals of 300 μm. Slides were then evaluated by a neuropathologist. For the remaining animals, the skull cap was isolated and preserved in formalin for subsequent testing.

4.2.2 Lesion formation in *Ex Vivo* Rats

Lesion formation was tested in a sacrificed Sprague Dawley female rat. After, the animal was sacrificed with CO_2 asphyxiation it was weighed. The weight of the rat was recorded at 256 grams and the animal head was prepared for the experiment. First, the head was shaved with electric Norelco clippers (Philips, Stamford, CT) and afterwards a depilatory cream was applied (Church & Dwight Co., Inc., Princeton, NJ). Second, to ensure a secure attachment to the motor, the head was separated from the body. To preserve the original position of the skin at the cut site, a layer of Loctite super glue (Henkel Co., Westlake, OH) was used to secure it. The head was then pinned to a rubber holder and secured to a 3-axis servomotor. The holder was then immersed inside a degassed, deionized water bath at room temperature (T = 24°C). Lesion formation was performed in the left side on the animal's brain; the right side served as a control where no therapy or imaging was performed.

Lesions were delivered in a systematic manner. First, the occipital bone was localized on the SA image. Figure 4.2(a) depicts the approximate location of the SA reference

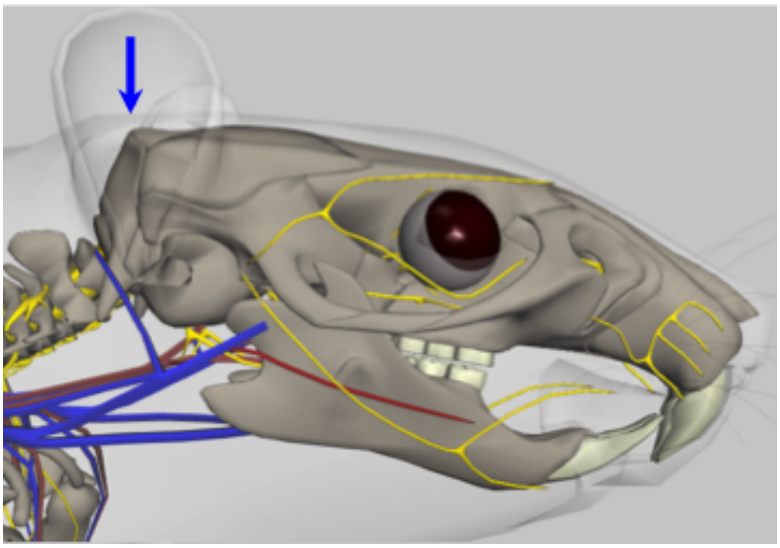

(a) Rat skull with the blue arrow depicting the approximate location of the reference plane used to visualize the occipital bone.

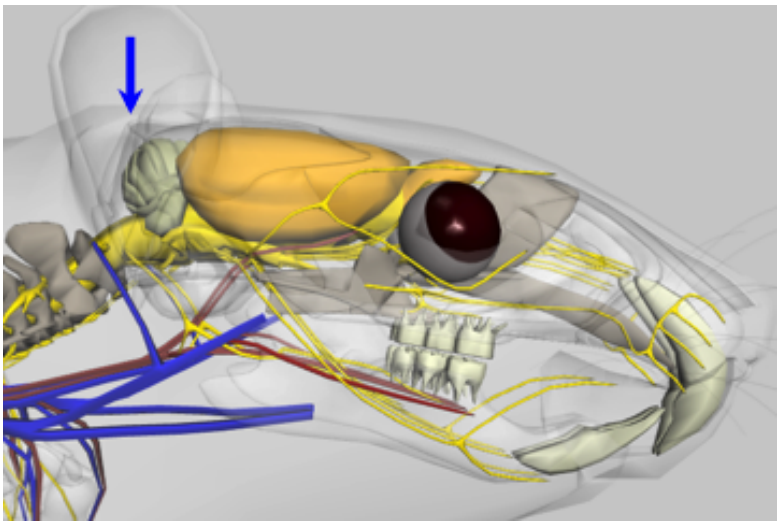

(b) The anatomical structures (cerebellum, cerebrum, and olfactory bulb) are visualized underneath the skull. The blue arrow depicts the approximate location of the reference plane used to visualize the occipital bone.

Figure 4.2: Visualization of landmarks for the transcranial lesion formation experiment.

plane, and Figure 4.2(b) illustrates the cerebellum, cerebrum, and olfactory bulb's positions underneath the skull. Both images were acquired from Rat Anatomy 3D software (Biosphera, Saint Charles, Brazil). Second, the therapy plane was located by moving 3 mm in the rostral direction from the occipital bone. Third, three different power levels (49 W, 64 W, 81 W) were tested with respective durations of 1.9 seconds, 1.1 seconds, and 0.7 seconds.

As depicted in Figure 4.3 17 lesions were created:

- 6 lesions at 81 W for 0.7 seconds, represented by red X's
- 6 lesions at 64 W for 1.1 seconds, represented by orange X's
- 5 lesions at 49 W for 1.9 seconds, represented by yellow X's

4.3 Results

4.3.1 DMUA Imaging and Subtherapy *In Vivo*

The *in vivo* experiments were carried out in eight female Sprague Dawley rats. The figures presented here are from the first two rats (rat A and rat B), with the results from rat A presented first. The cross-section of the targeted plane is seen in Figure 4.4(a), a hyperechoic structure is present at $\approx$ 38 mm. The axes of the image are aligned with the DMUA, where (x,z) = (0, 40)mm is the geometric focus of the array. The focal beam of the array was steered to (x, z) = (-1, 42)mm, and a subset of subtherapeutic shots were delivered, at five intensities: 0.25 W, 0.55 W, 1 W, 1.56 W, and 2.25 W.

The typical axial-temporal profile through the center focus is pictured in Figure 4.4(c). Localized heating was observed at $\approx$38 mm, 4 mm above the intended focus and at the location of the hyperechoic structure visualized on the SA image. The heating response was consistent with FUS ON and FUS OFF times. About 2 mm below the observed heating, evidence of a pulsating artery is seen, with a pulsation rate (180 beats per minute) consistent with the typical heart rate of a rat. Figure 4.4(c) summarizes temporal temperature traces at the location of the maximum temperature increase ($\approx$38 mm axially). For the low energy doses, the temperature rise was within the noise floor

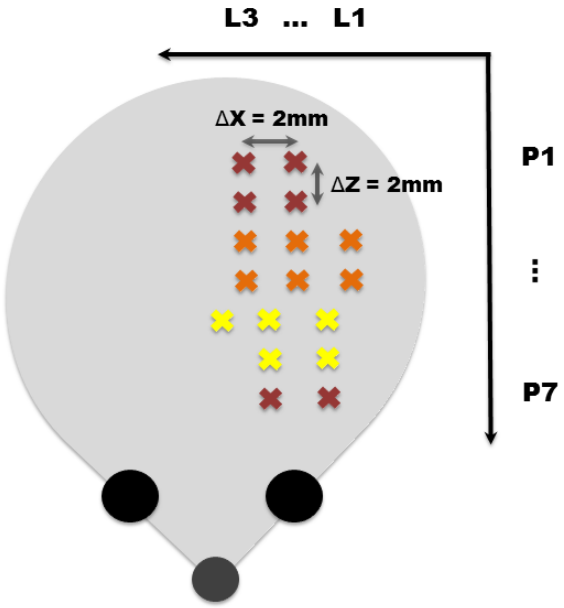

Figure 4.3: Matrix of Lesions formed in a Sprague Dawley Rat.

of the baseline; however, when a more distinctive ΔT was achieved at 1 W and higher, the shots were repeated three times to estimate the variance and repeatability of tFUS delivery and STF-based monitoring. The temperature traces reveal low variation for 1 W and 2.25 W, and more variability at 1.56 W.

In rat B, the therapy field is shown in Figure 4.4(b). Similar to rat A, a strong reflection is observed at $\approx$38 mm. The focus was located at (x, z) = (-1, 40)mm and the axial-temporal temperature profile is recorded in Figure 4.4(d). Shots were delivered at two acoustic powers, 1 W and 1.56 W. The higher acoustic power produced a spatial heating profile well above the baseline and as a result was repeated twice. The temporal variability for a 1.56 W shot was small (see Figure 4.4(f)), and the spatial heating response was very similar to the 1.56 W shot in rat A.

The results for the remaining 6 rats are not presented; however, the shots delivered produced similar responses to the results observed in rats A and B.

In summary, the *in vivo* experiments tied in with the *ex vivo* results presented earlier. Out of the 38 locations interrogated in eight animals, measurable temperature change was observed in all 38 cases, i.e. a sensitivity of 100%. The specificity of the observed response was 92%. In some cases, the peak temperature change was observed 2 mm proximal to the target. During bracketed delivery of subtherapeutic shots, the heating rate scaled linearly with delivered acoustic power. Repeatability of the temperature with low variance was established. The heating rate also agreed with experimental results presented earlier *ex vivo*.

In addition to localized temperature increases, the STF-based temperature imaging algorithm also revealed the presence of pulsation in the targeted regions. Figures 4.6 (a) and (c) depict strain data at a cross-section through the skull. The artery is located at 46 mm, and the respective arterial pulsation is evident on the trace seen in Figure 4.6(b). The data was collected at 400 fps. Increasing the sampling rate to 1000 fps revealed a more informative strain curve as seen in Figure 4.6(d), with evidence of a diastolic notch observed in 4 out of 4 pulsation cycles.

To further validate visualization of pulsating structures, the DMUA was used to image the heart. The animal was placed on its back, and the DMUA was centered on its

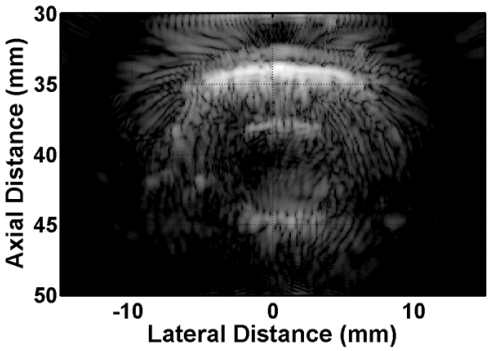

(a) Rat A: SA image

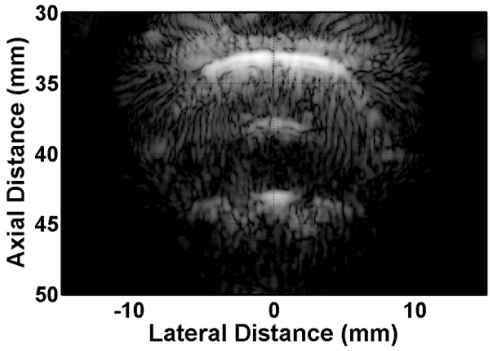

(b) Rat B: SA image

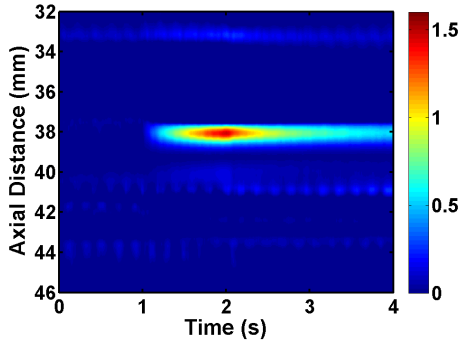

(c) Rat A: axial-temporal temperature

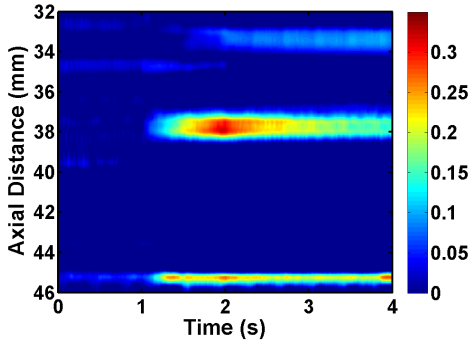

(d) Rat B: axial-temporal temperature

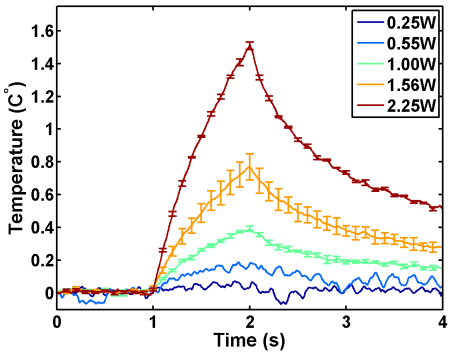

(e) Rat A: temperature

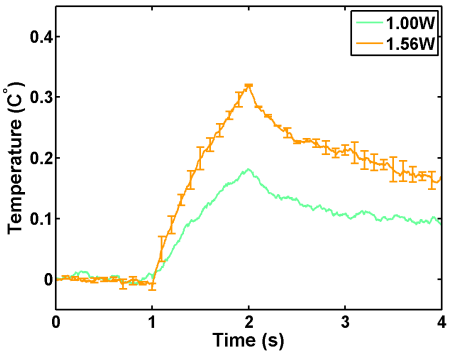

(f) Rat B: temperature

Figure 4.4: Results for *in vivo* STF-based thermography in rats A and B.

spinal column. Under the imaging guidance of the DMUA, the focus was positioned in cross-section with the heart, and the presence of strong pulsation was seen at the focus. The computed strain in Figure 4.6(f) resembles the strain common to a ventricle. As with the transcranial experiments, the pulsation was estimated at 180 beats per minute.

Safety and Efficacy of the *In Vivo* Treatment

Upon completion of the experiment all eight animals successfully recovered from the anaesthetic. During a three day recovery period, no physiological or behavioral deficits were observed. Also, ECG and body temperature data collected from the selected rats confirmed no apparent deviation of the vital signs from the normal baseline. Subsequent histological examination of tissue confirmed a lack of cellular damage and inflammation markers. These observations served as evidence that tFUS delivery results in only a low temperature rise. Therefore, shots delivered for 1 second in the range between 0.25-6.25 W are safe, even when repeated at 2 minute time intervals.

4.3.2 Lesion formation in *Ex Vivo* Rats

The objective of the transskull lesion formation experiment was to test transskull monitoring with STF imaging and to identify the duration and acoustic power needed for successful lesion formation. The objective was tested in a Sprague Dawley rat, where consistent doses of tFUS were delivered at 17 locations. The highest exposure was chosen as 81 W for a duration of 0.7 seconds; consecutive exposures are calculated to keep the therapeutic dose constant through a relationship of $C = I\sqrt{t}$ [47]. Only one of the 17 exposures created a clear lesion originating at the focus. The remaining 16 exposures exhibited either an immediate or a delayed response at the surface, obscuring evidence of change at the focal point. Figure 4.7 summarizes these results for three acoustic powers, with two examples for each power level.

Figure 4.5: Surface edema photographed after therapy completion. The ruler in the photographs correspond to a millimeter scale.

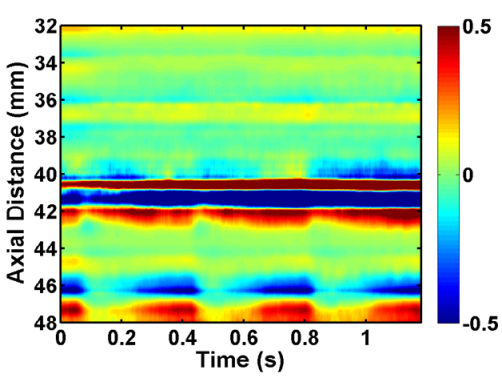

(a) Transskull: Temperature at 400 fps

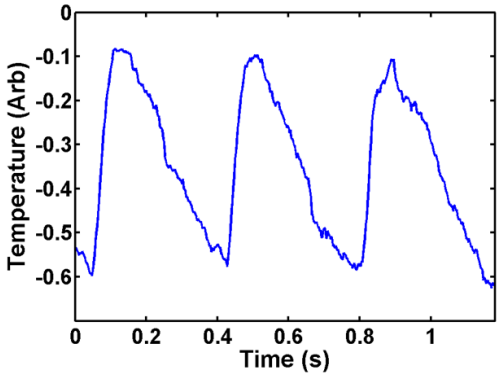

(b) Transskull: Strain trace of an artery

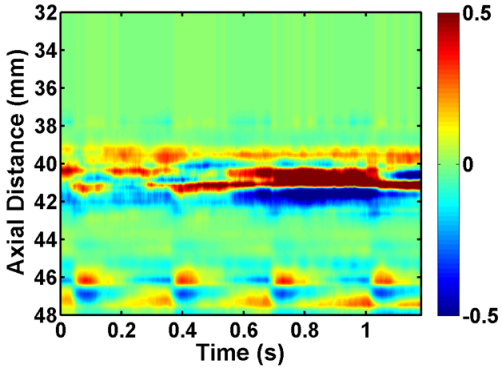

(c) Transskull: Temperature at 1000 fps

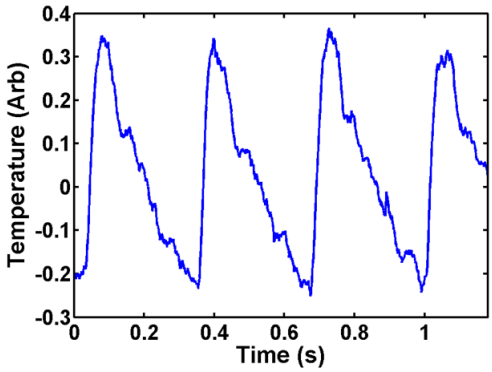

(d) Transskull: Strain trace of an artery

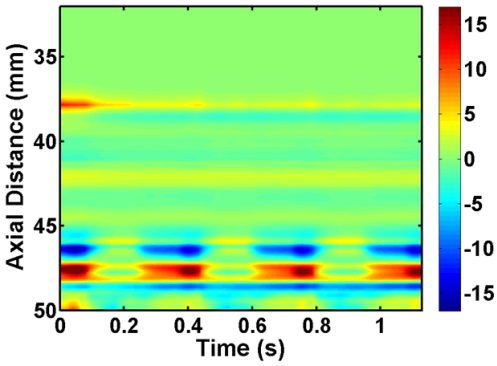

(e) Heart: Temperature at 1000 fps

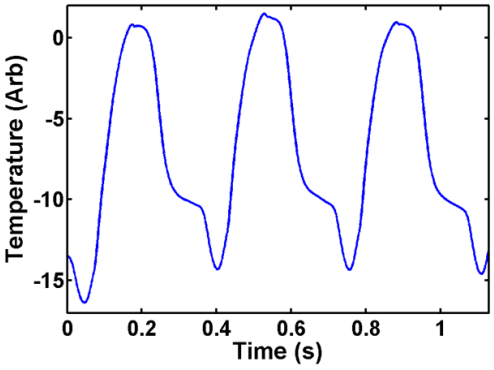

(f) Heart: Strain trace of a ventricle

Figure 4.6: Pulsation data recorded in rat B, where transskull imaging was done for (a), (b),(c) and (d); imaging of the heart was done in (e) and (f).

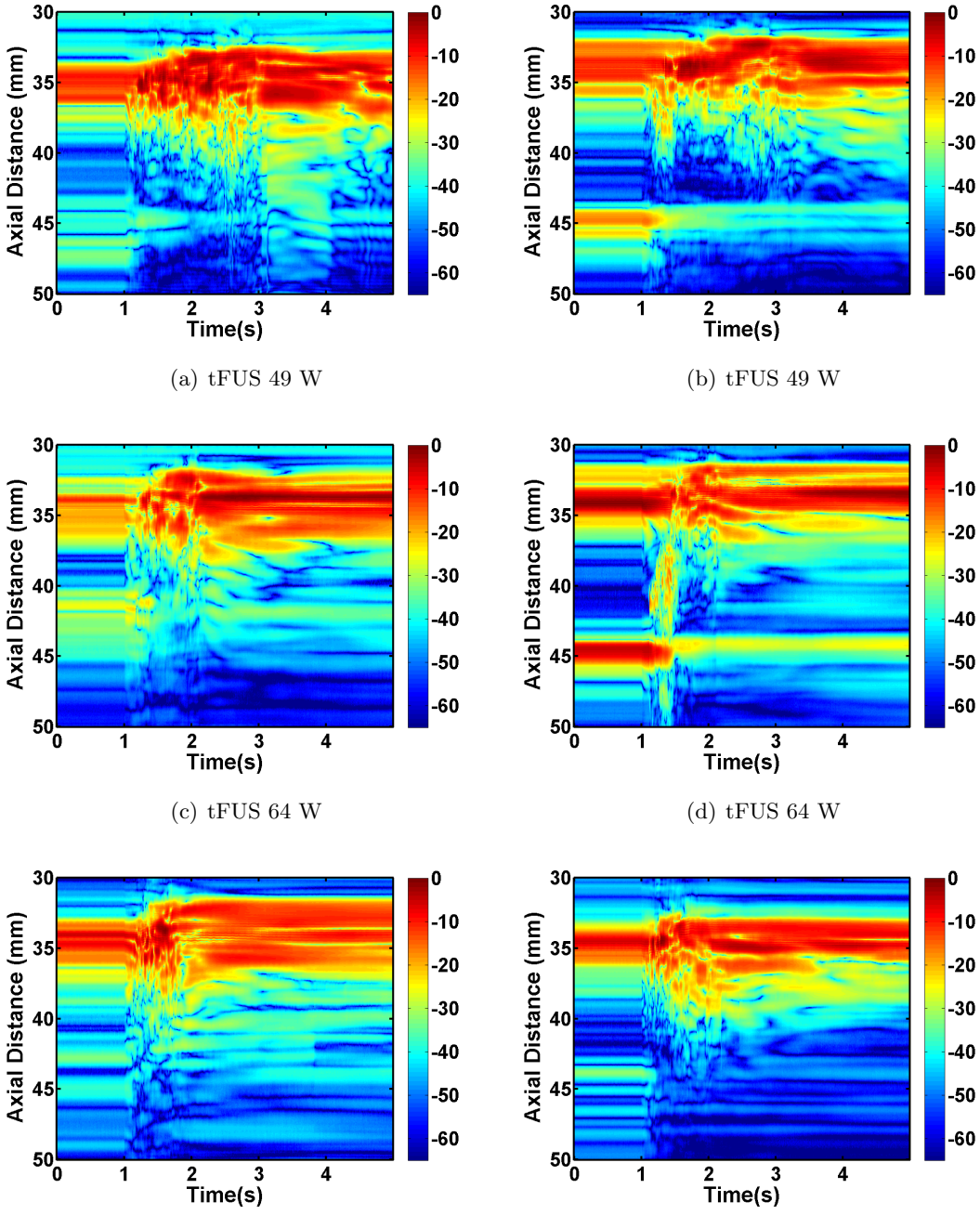

(a) tFUS 49 W

(b) tFUS 49 W

(c) tFUS 64 W

(d) tFUS 64 W

(e) tFUS 81 W

(f) tFUS 81 W

Figure 4.7: Lesion formation in a Sprague Dawley rat imaged with STF at three different power levels.

Figure 4.7(d) presents a clear example of the lesion formation process starting at the focal point, ≈40 mm axially, and growing toward the surface. This was the only indication of a lesion formed and it corresponded to a 64 W exposure for 1.1 seconds.

Figure 4.7(b) shows an example of a delayed response at the surface, which occurred in two instances at low exposure and high duration. After 500 ms the change at the surface started to shadow the focal point. This phenomenon originates from the appearance of bubbles blocking ultrasound waves from propagating deeper into the tissue.

The remaining 14 lesions showed an almost immediate echogenic change at the skin-skull interface, as seen in Figure 4.7(a), 4.7(c), 4.7(e) and 4.7(f). These figures also depict an immediate reduction in the echo prominence beyond activity at the skull surface.

Upon completion of the lesion formation protocol, the skin surface of the rat skull was examined for any visible damage. As seen in Figure 4.5, the rat exhibited a pronounced amount of surface edema.

Histological evaluation of the rat brain did not reveal any of the lesions observed under STF imaging. Based on the lack of damage seen upon histological examination, it is necessary to reevaluate lesion formation protocol parameters, taking into account the DMUA feedback. The echogenic change at the surface in 16 out of 17 cases, indicated significant heat build up at the skull interface. The inability to observe echogenic changes at the focal location 94 % of the time was consistent with the lack of histological damage. A new protocol needs to minimize the skull heating, as it compromises penetration of energy to the focus and also results in surface edema.

4.4 Conclusion

The feasibility of real-time image-guided placement and monitoring of tFUS beams using dual-mode ultrasound arrays was demonstrated in an *in vivo* rat model. Synthetic aperture imaging was used to guide the treatment procedure and identify important anatomical landmarks, such as the outline of the skull and skin layer. Furthermore, pulsating arteries within the field of view are often detectable on SA imaging. This is significant since vessels are often the target of potential transcranial therapies.

The results shown in this chapter have also demonstrated that real-time transcranial ultrasound thermography *in vivo* is capable of detecting and localizing the subtherapeutic tFUS heating profile with high spatial and temporal resolution. During the application of subtherapeutic tFUS patterns, with similar acoustic outputs, the heating rates estimated *in vivo* were consistent with those measured *ex vivo* using thermocouples. Some artifacts were observed on spatio-temporal temperature change profiles, but they neither obscured the actual heating pattern nor limited our ability to localize the tissue response to tFUS. Furthermore, STF-enabled monitoring revealed a significant amount of tissue change at the surface during the lesion formation process *ex vivo*. After the completion of treatment, surface edema was observed at the treatment site corroborating DMUA feedback.

Chapter 5

Characterization of Transcranial Focused Ultrasound Using DMUA Applications: *Ex Vivo Studies*

5.1 Introduction

Transcranial applications of focused ultrasound are often complicated by the presence of the skull. Due to the high variability between the speed of sound in the tissue and in the skull, the phase front emanating from the transducer becomes asynchronous and results in a deformed focus. The research presented in this chapter was conducted to characterize the degree of transcranial degradation of the DMUA focus. The characterization consisted of two complementary experiments. The first experiment was performed with two single-element transducers and allowed to estimate the amount of energy transmitted through the rat skull and optimal transmission frequency. The second experiment was conducted with a hydrophone and enabled visualization of the DMUA focus distortion through the skull at two different frequencies.

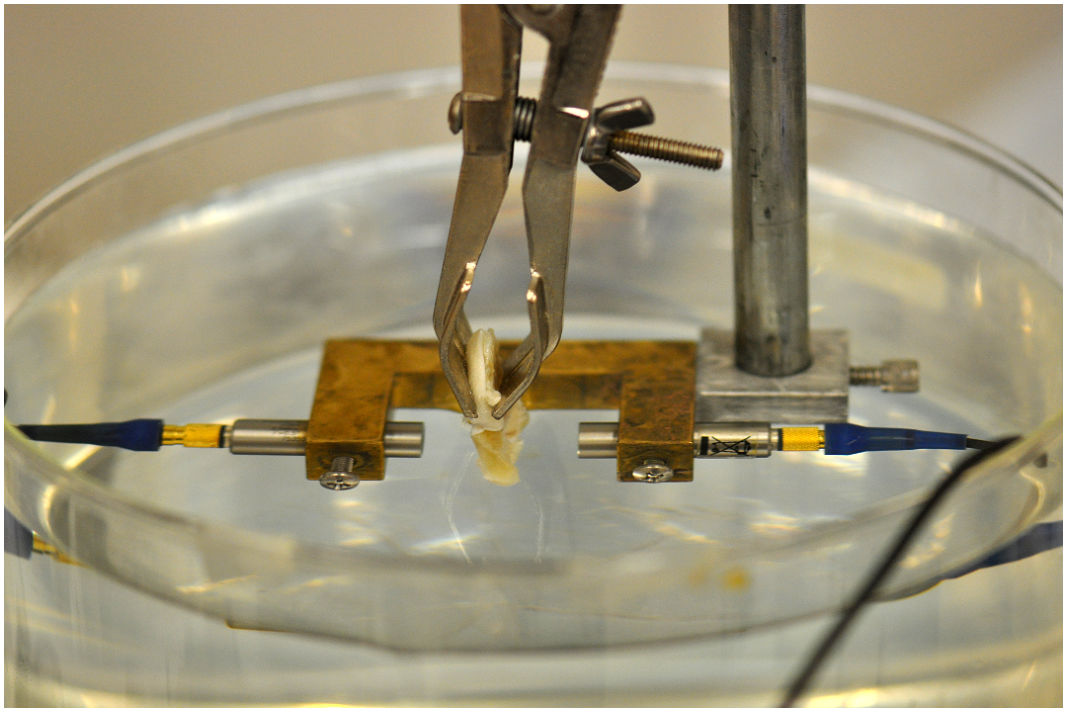

Figure 5.1: Experimental setup for the measurement of insertion loss through the skull.

5.2 Methods

5.2.1 Measurement of Insertion Loss Through a Rat Skull

To characterize the insertion loss through the skull in the frequency range 1.8 - 4.1 MHz, the setup shown in Figure 5.1 was used. Two single element transducers were placed in a brass holder 1 inch apart and facing each other. The holder was secured to a 3-axis servomotor. Each transducer had a center frequency of 3.65MHz (6dB bandwidth of 91.91%) and a focal length of 0.5 inches. The transducer facing the convex portion of the skull was operated in transmit/receive (T/R) mode enabling the collection of an echo waveform. The other transducer was operated in receive (R) only mode and was used to compute the relative insertion loss between the bone and water travelling paths.

The T/R and R transducers were connected to individual Panametrics pulser-receivers (Olympus, Tokyo, Japan). The outputs of both pulser-receivers were connected to an oscilloscope (Tektronix, Oregon, USA). The oscilloscope was setup to receive three channels:

- Channel 1: the received signal from the T/R pulser-receiver
- Channel 2: the received signal from the R pulser-receiver
- Channel 3: the trigger signal from the T/R pulser-receiver

To prepare the skulls for the procedure, the skin was removed and the upper portion of the cranium was separated with a bone band saw (Mar-Med Inc., Cleveland, OH, USA). The skull was then immersed in a saline bath to remove particulates and afterwards fixed in a 10% formalin solution. Fry and Barger [48] showed preserving the human skull in the formalin solution affected insertion loss measurement by only 3dB on average.

To estimate insertion loss, the skull was rinsed in tap water and positioned in a tank filled with degassed deionized water at a room temperature of 24°C. The skull was then scanned with an automated script written in MATLAB (MathWorks, Massachusetts, USA). The spatial resolution in the lateral and elevation dimensions was set to 0.25 mm. At each spatial location, 50 waveforms were averaged on the oscilloscope for the

T/R and R channels before being transferred to the PC via a GPIB interface. A delay of 10 seconds between each spatial acquisition was introduced to allow for the motor assembly to stabilize.

5.2.2 Data Analysis

The aforementioned experiment allowed the collection of two data sets: the topography of the skull and two-dimensional insertion loss estimates. These variables were extracted according to the following protocol:

- The topography of the skull was calculated based on the first arrival of the skull echo in the T/R waveform.
- Insertion loss was estimated from the frequency spectrum of the R waveforms, where the frequency spectrum of the reference waveform collected in water was subtracted from the frequency spectrum of the waveform travelling through the skull and water.

5.2.3 Hydrophone Characterization of a DMUA Focus

To characterize DMUA beam deformation through the skull, we conducted a hydrophone study. The study was performed on a formalin-fixed skull, harvested from a 281 g Sprague-Dawley female rat.

The first step of the characterization procedure was to map the pressure of a DMUA field in water. The hydrophone was immersed in a water tank with degassed water, and positioned with the guidance of SA imaging at the focal point of the DMUA. The signal captured by the hydrophone was amplified with an AH-2010 preamplifier and acquired by an oscilloscope with a sampling rate of 50 MHz (Tektronix, Oregon, USA). The hydrophone was secured onto a 3-axis servomotor stage. After each change in the hydrophone location, the DMUA system was programmed to emit a (120mV) 32 cycle burst with a center frequency of 3.2MHz and to transmit a trigger signal to the oscilloscope. The oscilloscope transferred received waveforms to the PC via a GPIB interface.

To ensure the accurate acquisition of the DMUA pressure field, three scans were acquired with the hydrophone:

1. First, a scan of the lateral-elevation plane starting at the approximate axial-lateral DMUA focal center was used to find the lateral-elevation pressure maximum. To locate the approximate axial-lateral DMUA focal center, SA imaging was used to visualize the hydrophone tip positioned at the focal point. The DMUA focal field was sampled in the lateral-elevation plane over a lateral range (-2.6mm to 2.6mm) at 0.05 mm increments and an elevation range (-2.6mm to 2.6mm) with 0.1mm increments with the motor speed set at 2 mm/s.

2. Second, a scan of the axial-lateral plane starting at the lateral-elevation maximum was done to find the axial pressure maximum. The DMUA focal field was sampled in the axial-lateral plane over an axial range (-7 mm to 7 mm) at 0.1 mm increments and lateral range (-2.8 mm to 2.8 mm) with 0.05 mm increments. The motor speed was reduced to 0.5 mm/s to ensure accurate signal capture at each spatial location.

3. Third, a scan of the lateral-elevation plane was done starting at the determined pressure maximum in the axial dimension. The DMUA focal field was sampled in the lateral-elevation plane over a lateral range (-2.8 mm to 2.8 mm) at 0.05 mm increments and an elevation range (-2.8mm to 2.8mm) with 0.1 mm increments with the motor speed set at 0.5 mm/s.

After the acquisition of the DMUA pressure field in water, the skull was introduced between the DMUA and the tip of the hydrophone as seen in Figure 5.2(a). Figure 5.2(b) depicts the approximate elevation location of the measurement through the skull. As with the *in vivo* experimental setup, the axial placement of the skull was at 32 mm on the SA image, such that the focal point was located 8 mm behind the bone. Three different lateral configurations were tested: the midline, 2 mm to the left of the midline and 2 mm to the right of the midline.

For each configuration, axial-lateral and elevation-lateral hydrophone scans were acquired with the same protocol as described for water. The only difference was that the axial scanning range was reduced to ensure the hydrophone tip did not touch the

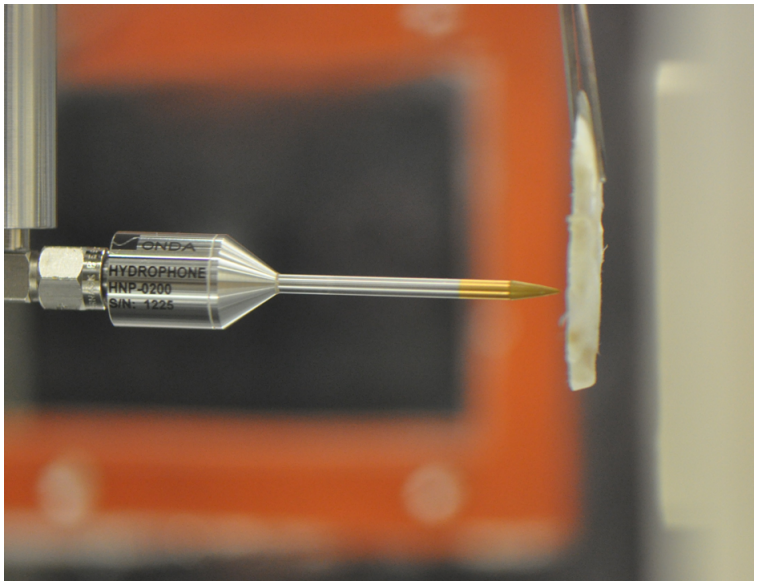

(a) Hydrophone facing the skull

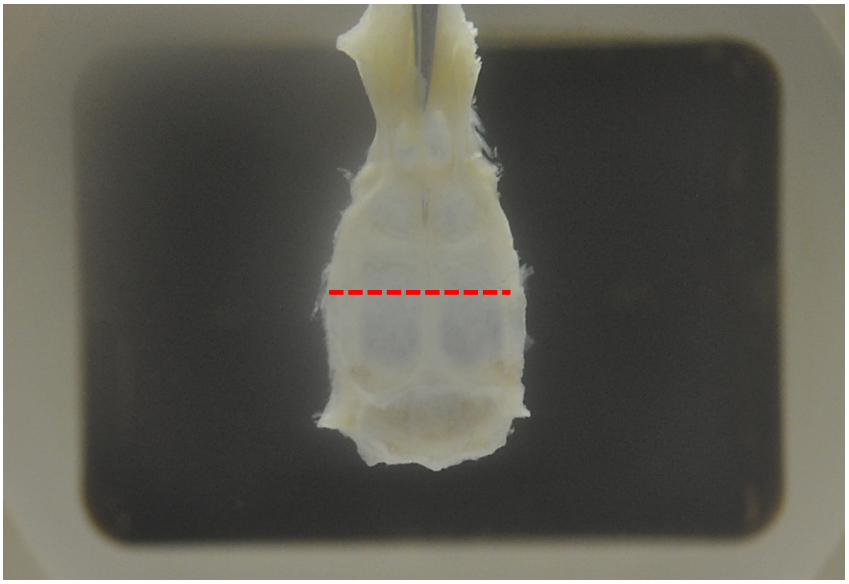

(b) Skull positioned in front of DMUA

Figure 5.2: Experimental setup of the hydrophone scan of the DMUA focus through the skull. The red line in (b) represents the center of the DMUA surface in the elevation dimension.

skull.

Characterization of the DMUA Focal Beam for Varying DMUA Frequencies

We also investigated the pressure field profile as a function of different DMUA transmit frequencies. For this experiment two frequencies (1.8 MHz and 3.2 MHz) were tested with and without the skull. These hydrophone scans were acquired with the same protocol as described for water.

5.3 Results

5.3.1 Insertion Loss Study

The goal of this study was to determine the insertion loss as a function of location and frequency. The results of the insertion loss study were examined in a systematic manner, starting with an inspection of the skull orientation with respect to the transducer. This orientation was of significance, because the curvature of the skull affected how incident waves were scattered at the skull. The skull surface geometry computed from the echo waveforms for rats A and B is displayed in Figures 5.3(a). In both cases the orientation of the skull was approximately symmetrical along the zero lateral parallel, allowing for the investigation of insertion loss through the skull.

Next, we examined the amplitude spectra at different frequencies with and without the skull. For a more complete picture of insertion loss through the skull, three unique locations were chosen for examination:

1. (x1, y1) = (0 mm, 10 mm)
2. (x2, y2) = (0 mm, 15 mm)
3. (x3, y3) = (2 mm, 10 mm)

The resulting amplitude spectra for water and skull waveforms, as depicted in Figure 5.3(b), showed two notable features.

- First, a significant reduction in amplitude spectra was observed for traces transmitted through the skull with the trace at location (x2, y2) exhibiting the most pronounced loss.
- Second, the pronounced frequency dependence of the amplitude was not consistent between locations. For example, in the frequency range from 2.2 to 3.5 MHz, the amplitude spectra behaved differently at the three locations, whereas below 2.2 MHz and above 3.5 MHz the amplitude spectra were strictly increasing and strictly decreasing, respectively.

For a more thorough understanding of ultrasonic penetration, we examined the spatial power loss results computed at three frequencies (1.8 MHz, 3.2 MHz, and 4.1 MHz). At 1.8 MHz the insertion loss was relatively consistent over the area of the skull as seen in Figure 5.4(a). At the higher frequencies, 3.2 MHz (Figure 5.4(b)) and 4.1 MHz (Figure 5.4(c)), the insertion loss was more spatially dependent. These spatial dependencies seemed to correlate with the gross anatomical features shown in Figure 5.5. In both rats A and B, there was more insertion loss on the right side of the skull. A minor deviation in orientation of the skull, nonuniform skull thickness, or an asymmetrical cutting of the skull could explain this asymmetry.

5.3.2 Hydrophone Characterization of a DMUA Focus

To follow up on the results observed *in vivo* we conducted experiments to answer four questions:

1. How does the skull affect the DMUA beam resolution?
2. How much power is lost due to the presence of the skull?
3. How are questions 1 & 2 affected by mechanical adjustments and electronic steering of the focus?
4. How are questions 1, 2, & 3 affected by changes in the DMUA frequency?

Subsequent sections are geared to answer these questions by scanning the DMUA field with a hydrophone and examining its beam profile with and without the skull.

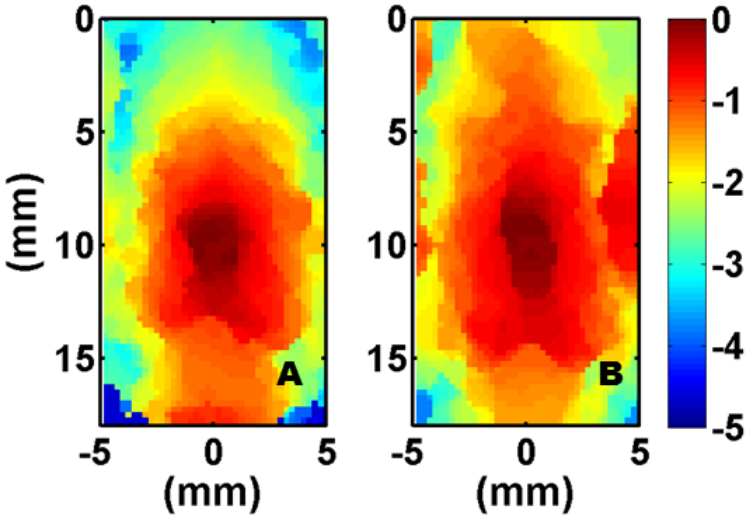

(a) Skull topography for rats A and B

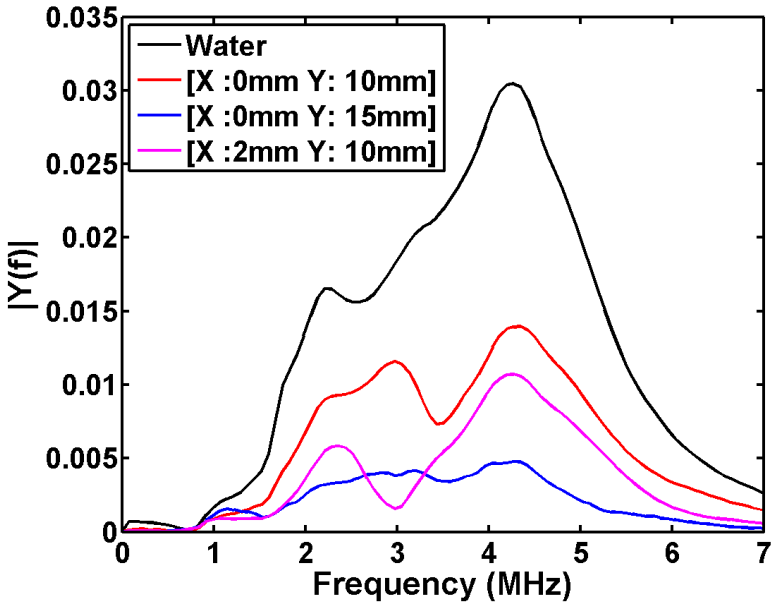

(b) Frequency spectrum of the transmitted pulse through water and three different locations in rat A skull

Figure 5.3: Topography maps of the skulls from rats A and B are depicted in (a), and the frequency spectra of the transmitted pulses are depicted in (b).

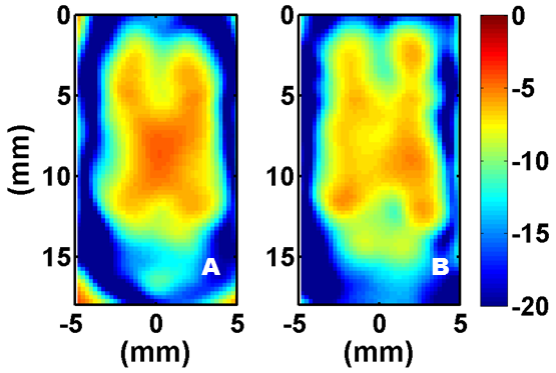

(a) 1.8 MHz

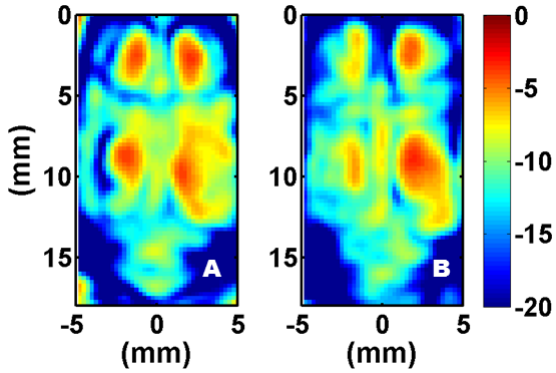

(b) 3.2 MHz

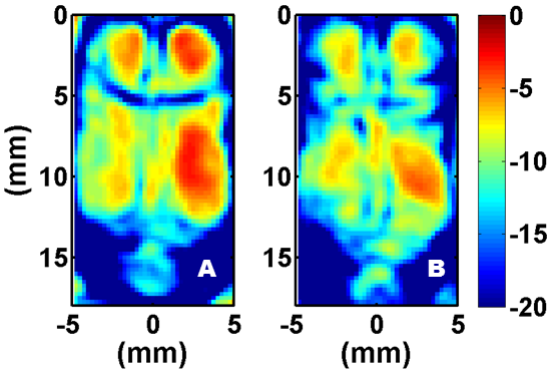

(c) 4.1 MHz

Figure 5.4: Insertion loss in dB measured at three frequencies (1.8 MHz, 3.2 MHz, and 4.1 MHz) for two rats (A and B).

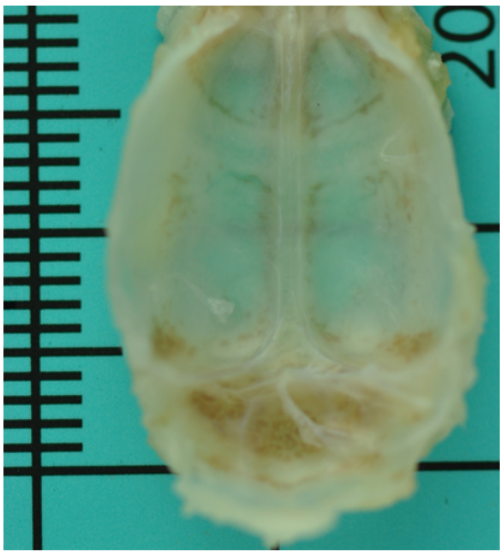

(a) Rat A

(b) Rat B

Figure 5.5: Inferior view of the upper portion of the skulls from rats A and B.

Beam Resolution with and without the Skull

Hydrophone scans were conducted to visualize axial-lateral and elevation-lateral cross-sections of the DMUA beam in the water, with and without the skull. At the start of the data acquisition, the hydrophone was first localized on the SA image. Figure 5.6(a) depicts the tip of the hydrophone at the (x, z) = (0 mm, 40 mm) location inside the water. When the skull was positioned in front of the DMUA, the hydrophone tip could still be visualized (see Figure 5.6(b)); however, the original resolution was degraded. This observation was consistent with our previous results from the wire phantom study, presented in section 3.3.2.

Figures 5.7(a) and 5.7(b) depict axial-lateral beam profiles in water and through the skull. The skull resulted in a spreading of the beam energy and reduced the focal gain revealing pre-focal sidelobes. The deformation of the focused beam was noticeable both the in axial and lateral dimensions when the skull was introduced (see Table 5.1[1]). This observation is in line with previously documented temperature profiles *in vivo*, where the heating was often observed 2 mm proximal to the target.

Power Loss Through the Skull

An accurate estimate of the power loss due to the reflection and absorption of the skull is necessary to estimate how much power can be gained through refocusing. To estimate power loss, the intensity was integrated over the elevation-lateral plane (-2.5 mm to 2.5 mm in both dimensions) both with and without the skull. The difference between the power with the skull and the power without the skull was 6.8 dB and represented the power lost due to reflection and absorption.

Furthermore, we examined maximum intensity values with and without the skull to see if the difference in these values were comparable to the power loss estimates. By comparing the maximum intensity with and without the skull we observed a difference of 9.1 dB. As we already determined that only 6.8 dB of this loss was due to reflection and absorption, optimally 2.3 dB of intensity could be gained through refocusing. Since the

[1] Lateral and elevation resolution values were not corrected for the effect of the finite size of the hydrophone.

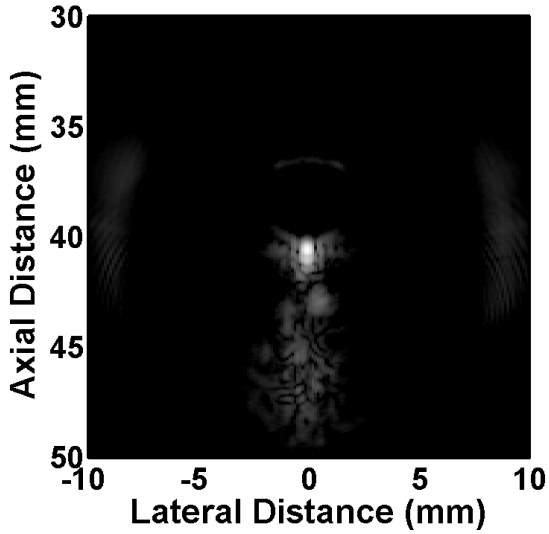

(a) SA image without the skull (55dB)

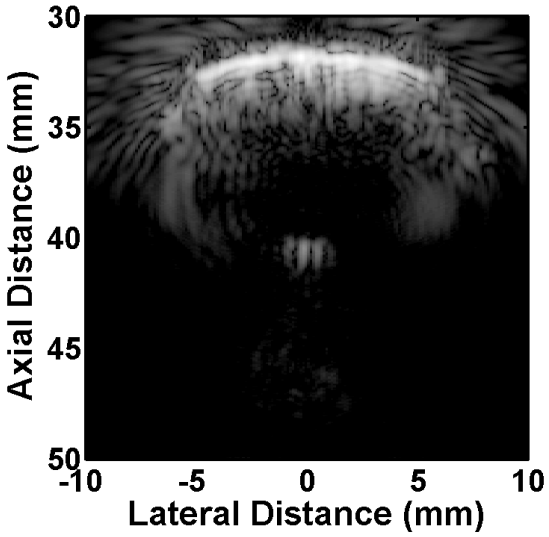

(b) SA image with the skull (55dB)

Figure 5.6: SA images of the hydrophone tip without (a) and with the skull (b) in water.

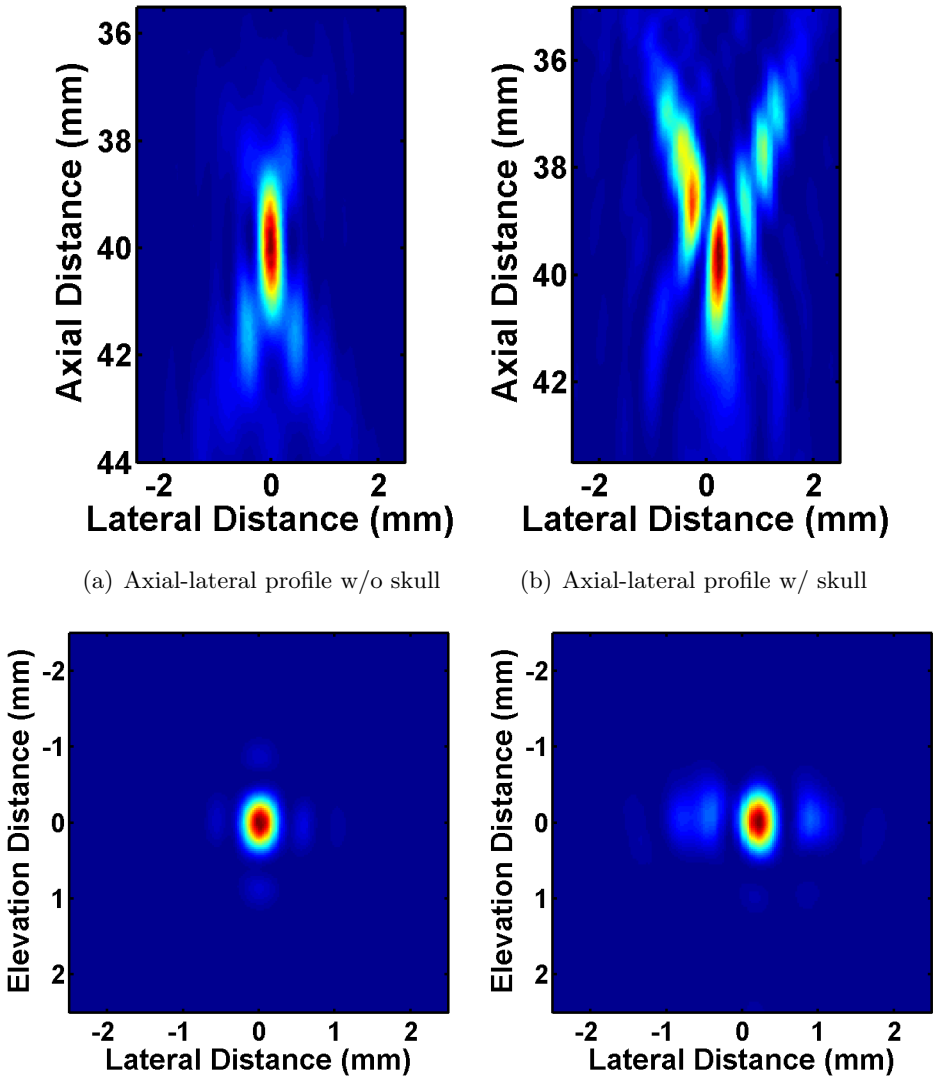

(a) Axial-lateral profile w/o skull

(b) Axial-lateral profile w/ skull

(c) Elevation-lateral profile w/o skull

(d) Elevation-lateral profile w/ skull

Figure 5.7: DMUA normalized intensity profiles with and without the skull.

maximum intensity is directly proportional to the heating rate at the focus, improvements in the focal intensity would allow a minimization of both the pre-focal heating and the acoustic power necessary to cause a desired change during subtherapeutic and therapeutic exposures.

Mechanical Adjustment vs Electronic Steering of the DMUA beam

Up until now the hydrophone scans were performed by aligning the midline of the skull symmetrically with the DMUA surface. In this section we investigate the effect of either electronically steering the beam or mechanically positioning it ± 2 mm off the midline. Figures 5.8(a) and 5.8(b) depict the results of DMUA beam electronic steering, whereas Figures 5.8(c) and 5.8(d) represent the mechanical movement of the skull in respect to the DMUA focus. The beam profiles with mechanical adjustment and electronic steering were spatially similar to each other, such that the imprecision of the mechanical movement could explain all of the deviation (mechanical displacement was precise within 1 mm). This spatial similarity and imprecision of mechanical adjustment suggests that electronic steering could be advantageous, particularly because it requires less time, keeps the same configuration between probe and the targeted organ, and is more spatially precise. However, a comparison of the resolution and power levels between mechanical adjustment and electronic steering (see Table 5.1) provided contradicting resolution and power loss results. Because this is a small data set, the results presented here should be used as a guide to further investigation.

Table 5.1: DMUA beam resolution without and with the skull

DMUA Freq. (MHz)	Focus [Ax; Lat.] (mm)	Water/ Skull	Axial DoF (mm)	Lateral Resol. (mm)	Elevation Resol. (mm)	Acoustic Intensity (W/cm^2)	Power (W)
1.8	[40; 0]	Water	4.537	0.850	1.237	4.538	198
3.2	[40; 0]	Water	2.962	0.487	0.712	217.143	3492
4.1	[40; 0]	Water	2.375	0.393	0.571	83.870	875
1.8	[40; 0]	Skull	5.312	0.829	1.238	0.953	41
1.8	[40; -2]	Skull	> 8	1.253	1.459	0.352	31
1.8	[40; 2]	Skull	4.927	1.107	1.450	0.480	36
3.2	[40; 0]	Skull	3.106	0.483	0.825	26.688	717
3.2	[40; -2]	Skull	4.543	0.661	0.927	17.516	607
3.2	M [40; -2]	Skull	5.539	0.653	0.904	19.265	606
3.2	[40; 2]	Skull	5.094	0.608	1.440	16.832	736
3.2	M [40; 2]	Skull	3.883	0.854	0.815	19.393	691

DMUA Transmit Frequency: 1.8MHz vs 3.2MHz

The final point of investigation was frequency choice for the transcranial experiments. First, we examined the DMUA focal resolution at the midline location for the two frequencies, as depicted in Figures 5.9(c) and 5.9(d). It is evident that at 1.8 MHz the beam is more localized, and the prefocal sidelobes are less pronounced. However, the use of the refocusing algorithm at 3.2 MHz could potentially restore its superior resolution.

Electronic steering the beam to $\pm$ 2 mm changed the profile of the beam significantly for both frequencies, as seen in Figure 5.10. In Figure 5.10(b) the axial resolution of the beam at 1.8 MHz exceeds 8 mm, which is almost the length of the skull ($\approx$ 10 mm) cross-section. Using a frequency which produces a small interrogation location, reduces the risk of standing waves in the skull and helps achieve a more targeted therapy. As a result, 1.8 MHz was not an optimal choice for localized transcranial applications.

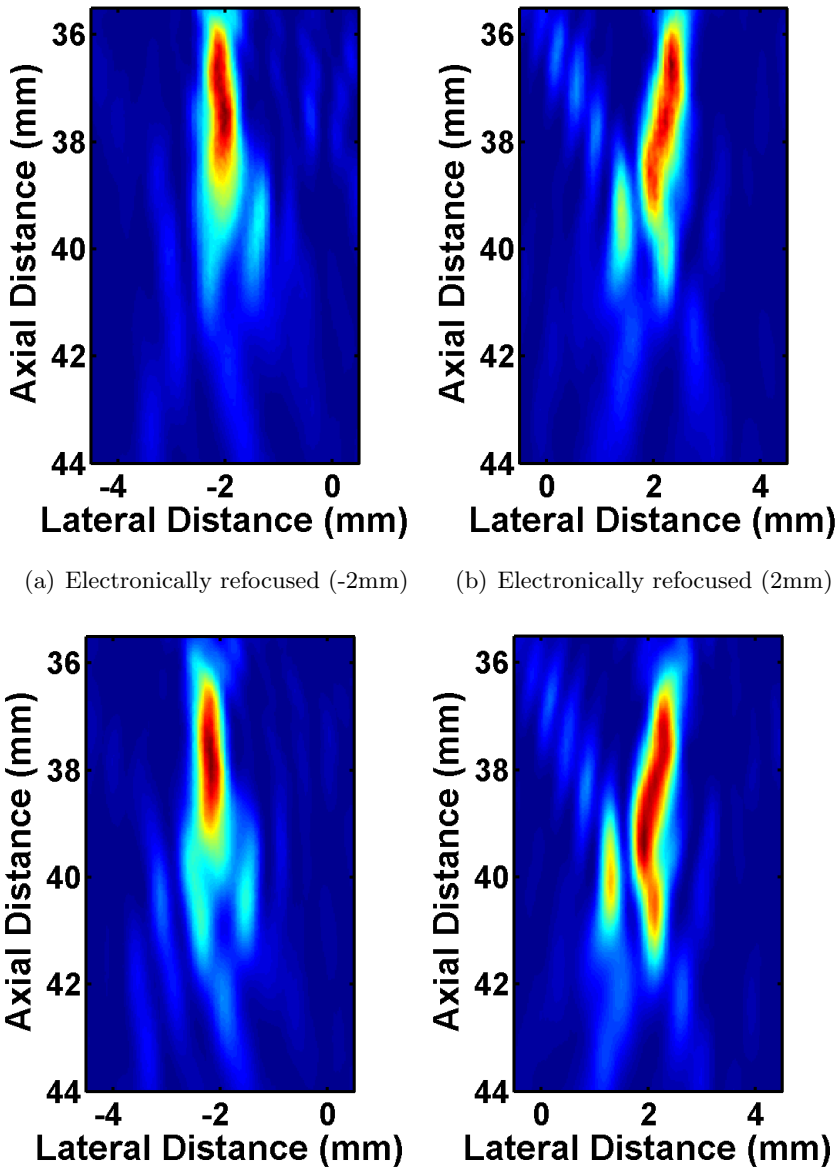

(a) Electronically refocused (-2mm)

(b) Electronically refocused (2mm)

(c) Mechanically moved (-2mm)

(d) Mechanically moved (2mm)

Figure 5.8: Hydrophone scans of DMUA focus through a skull of a Sprague-Dawley rat. Electronic refocusing is compared to a mechanical translation of the skull to a new location.

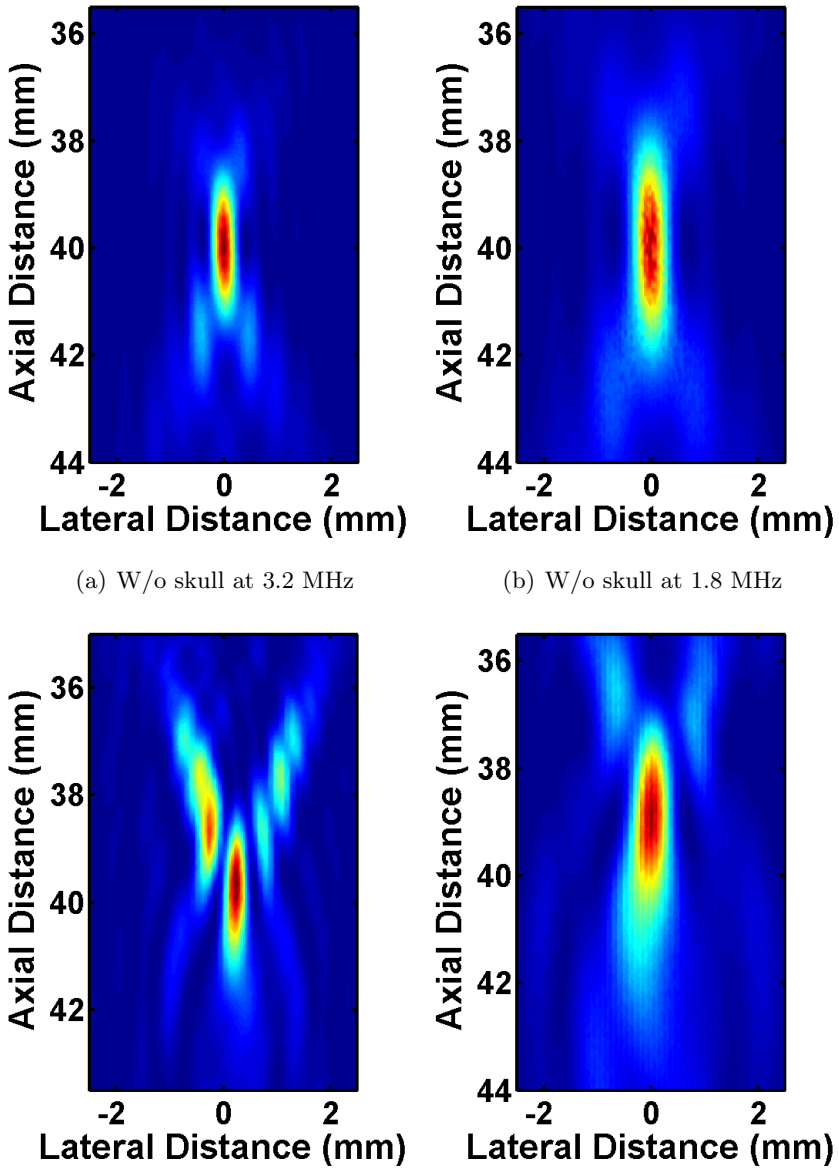

(a) W/o skull at 3.2 MHz

(b) W/o skull at 1.8 MHz

(c) With the skull at 3.2 MHz

(d) With the skull at 1.8 MHz

Figure 5.9: DMUA Focus with and without the skull at two different frequencies (1.8 MHz and 3.2 MHz).

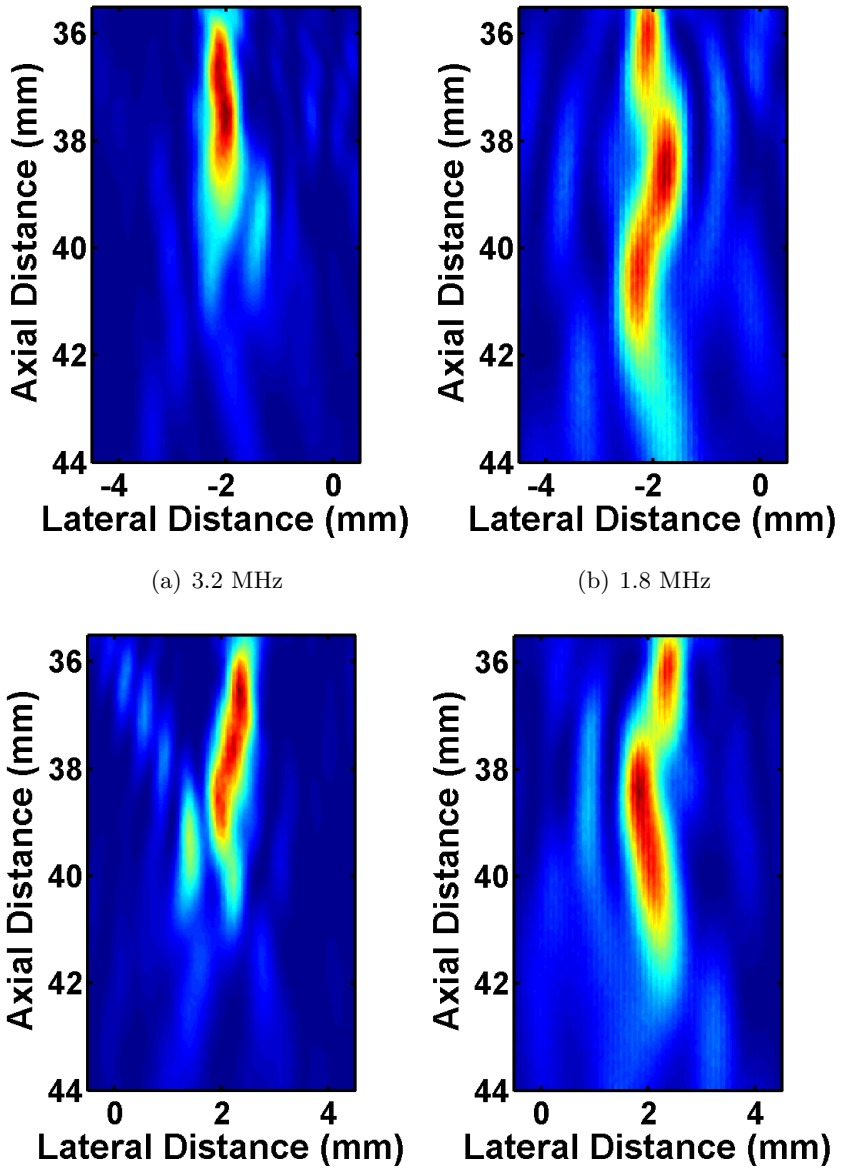

(a) 3.2 MHz

(b) 1.8 MHz

(c) 3.2 MHz

(d) 1.8 MHz

Figure 5.10: DMUA focus steered ±2 mm of the midline at two different frequencies (1.8 MHz and 3.2 MHz).

At last, we compared the power loss at 1.8 MHz with and without the skull in water. The value of the power loss was equal to 6.8 dB, and was in close agreement with the value previously computed for 3.2 MHz.

Conclusion

In this chapter we examined insertion loss through the rat skull and observed the variability of the estimate both in space and as a function of frequency. The frequency of 3.2MHz was validated as appropriate for maintaining focus and avoiding interference patterns from the back of the skull. Additionally, we have learnt that different locations exhibit different focal distortions. The degree of distortion was less pronounced when the skull was symmetrically aligned with the DMUA. Electronic steering of transcranial focused ultrasound beams does not appear to produce more distortions than mechanical adjustment of the focus. Presented results confirm that although the skull introduces a measurable distortion, the focus is still localized, enabling the measurement of transcranial FUS-tissue interactions with the DMUA.

Chapter 6

Localized Assessment of HIFU-induced Changes in Tissue Properties

6.1 Introduction

As the notion of focused ultrasound (FUS) as a noninvasive alternative to conventional surgery is becoming more widely accepted, the need for reliable quantitative feedback to assess thermal damage is growing. The dual-mode ultrasound array was designed to form a highly localized heating spot. When this functionality is combined with the ultrasound thermography the operator gains the ability to make a localized noninvasive measurement at a subtherapeutic exposure level.

In this study we expand on previous research in [39], by estimating the initial heating rate before and after therapeutic lesion formation through the delivery of a subtherapeutic intensity shot in *ex vivo* bovine heart tissue and an *in vivo* rat. Careful gross examination of the tissue confirms the measurement for every location where quantitative estimates were taken.

6.2 Methods

6.2.1 System Description

Subtherapeutic and therapeutic shot delivery and imaging were enabled by a custom designed platform with a 3.5 MHz DMUA (Imasonic, Besancon, France). The experiments were conducted in a water tank with the DMUA attached to one side facing a piece of tissue in a rubber holder as shown in Figure 6.1b. Precise movement of the tissue block was enabled by a motorized stage. Both the tissue and water were kept at room temperature. During shot delivery STF images were collected at 140 fps. STF-based thermography enabled the estimation of the temperature profile used to extract the initial heating rate.

6.2.2 Absorption Measurement

The method use to determine the rate-of-heating, shown in [49], was derived from the Pennes bioheat transfer equation (6.1).

$$\rho_t C_t \frac{\partial T}{\partial t} = k_t \nabla^2 T - w_b C_b (T - T_\infty) + 2\alpha I \tag{6.1}$$

where ρ_t is tissue density, C_t the specific heat of the tissue, T the tissue temperature, t time, k_t the thermal conductivity of the tissue, w_b the blood perfusion rate, C_b the specific heat of blood, T_a the arterial blood temperature, α the absorption coefficient of the tissue, and I the local ultrasonic intensity.

When the initial heating rate measurement is done shortly after the start of therapy, tissue diffusion and perfusion are negligible. This allows for the simplified version of the Pennes bioheat equation as seen in equation 6.2. This equation includes an initial heating rate proportional to the local ultrasonic intensity, as well as the tissue density, specific heat and absorption coefficient.

$$\frac{dT}{dt} \approx \frac{2\alpha I}{\rho_t C_t} \tag{6.2}$$

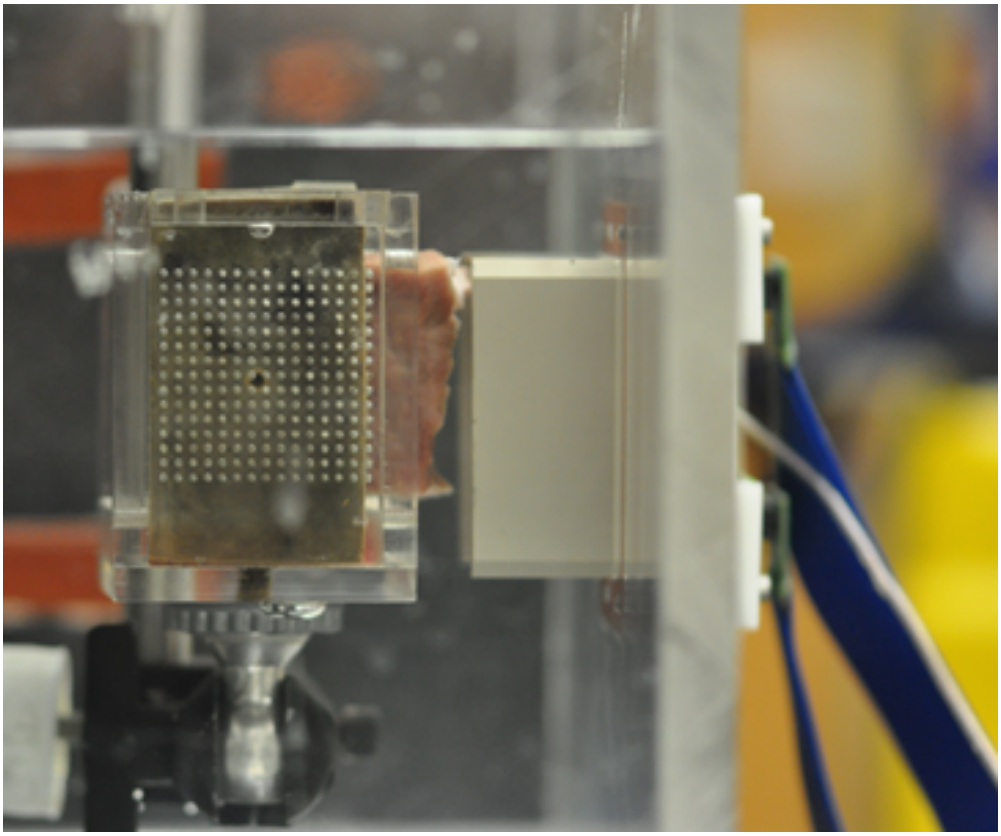

Figure 6.1: The DMUA is submerged inside a water tank facing a piece of bovine heart tissue.

To estimate the appropriate power levels for the subtherapeutic shot delivery, we first determined the relationship between voltages and the power output using an ultrasound power meter (Ohmic Instruments, Easton, MD). Additional calibration was conducted in bovine heart tissue with a 200 μm T-type copper-constantan thermocouple (Omega, Stamford, CT). After the calibration, a set of 1 second subtherapeutic shots was delivered 12 mm deep in the bovine heart tissue. The set contained five distinct acoustic intensities: 140 W/cm^2, 250 W/cm^2, 390 W/cm^2, 560 W/cm^2, and 760 W/cm^2. These subtherapeutic shots were repeated twice, first in increasing intensity levels (140 W/cm^2, 250 W/cm^2, etc.) and second, in decreasing intensity levels (760 W/cm^2, 560 W/cm^2, etc.) prior to lesion formation. After subtheraputic shots, volumetric lesion was formed using electronic steering with the DMUA. In tissue block # 1, the volumetric lesion was composed of 5 electronically steered foci spaced .55 mm apart (1350 mW/cm^2), with each shot ON for 200ms at a location before rotating to the next location, for a total duration of 5 seconds (Figure 6.2a). After the completion of therapy, the subtherapeutic shots were repeated. In tissue block #2, lesion parameters were the same, except the foci were spaced 0.50 mm apart (Figures 6.2b and b1).

Once the temperature data was extracted, the initial heating rate estimates were computed for the first 300 ms after the start of subtherapeutic exposure. The temperature probing location was chosen by finding the maximum temperature increase along the lateral axis within +/- 3 mm of the geometric focus in the axial dimension.

6.2.3 Noninvasive IgFUS with the *In Vivo* Small-animal Model

Trackless lesion formation was performed in the hind limb of Copenhagen rats in accordance with approved protocol (UMN IACUC #1101A94814) and UST was performed using the DMUA and SonixRP integrated system (section 2.1). A 3.5 MHz concave transducer array (40-mm radius of curvature) was used to generate FUS beams with dimensions of $0.2 \times 0.4 \times 2\text{mm}^3$ in the lateral, elevation, and axial dimensions, respectively. The therapy array has a fenestration that allowed for the use of a diagnostic probe for real-time imaging of the tissue with the imaging slice aligned with the FUS beam in the lateral and axial directions. The animal was placed in a temperature-controlled water bath with its hind limb positioned so that the focal spot of the therapy array was 6 -

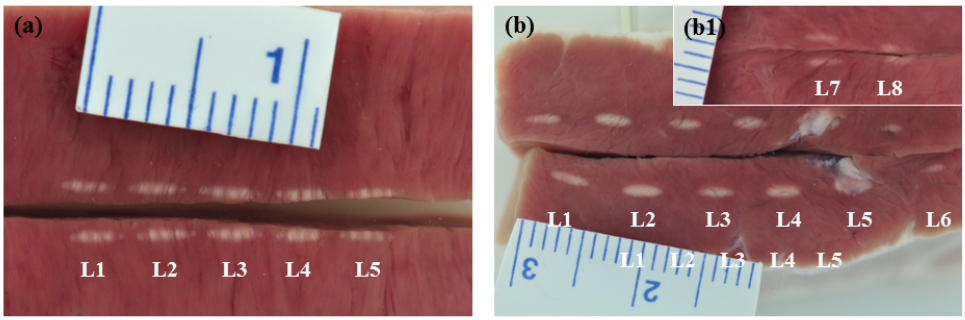

Figure 6.2: Gross images of lesions formed in Block # 1 (a) and Block # 2 (b). These images capture tissue cross-sections in the lateral-elevation plane with respect to the transducer beam axis.

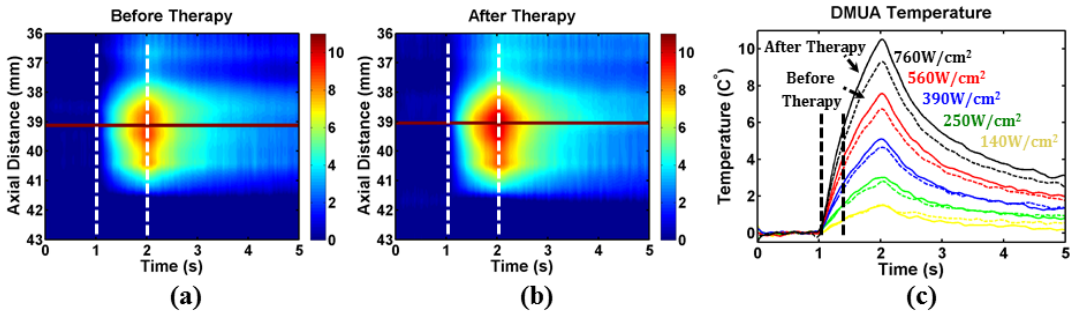

Figure 6.3: The temperature collected during subtherapeutic shots acquired at 760 mW/cm^2 before (a) and after (b) therapy, with the red line depicting the capture location of the temperature traces plotted in (c). In (c) the dotted lines represent the measurements made before therapy, and the solid lines represent measurements made after therapy.

10 mm under the skin.

A typical lesion formation procedure involved the use of two subtherapeutic FUS beams before and after the therapeutic beam, all with the same duration but differing in intensity. The subtherapeutic beam intensity was chosen to produce a 1 - 3°C change at the intended lesion location. Two discrete lesions were formed in one or more planes before the animal was removed from the water bath and allowed to recover for 4 hours before sacrifice. After sacrifice, the rat was perfused intracardially with 120 ml of saline, 190 ml of nitro blue tetrazolium (NBT) and 120 ml of 10% formalin. The formalin-fixed right leg was scanned using two modalities: a SonixRP US scanner with an L14-5/38 probe and a 9.4 Tesla MRI with a voxel size of $0.14 \times 0.14 \times 0.27\text{mm}^3$. For the 3D scan with SonixRP, the probe was positioned on a Vexta stepping motor (PK266-03A-P1). The fixed tissue was then sliced at ≈ 3 mm intervals, photographed and submitted for further histological processing.

6.2.4 UST and Tissue Property Measurement

Real-time UST images were formed using the system described in section 2.1. Briefly, beamformed RF data from a limited frame around the heated region (referred to as M2D data) was obtained using the diagnostic probe connected to the Sonix RP scanner. M2D-mode imaging allowed for the use of frame rates in the range of 80 - 500 fps, which proved suitable for capturing the full dynamics of tissue motion and deformation using speckle tracking techniques as described in [42] and references thereof. For the current experiment, M2D frames were acquired at 91 fps which allowed for the capture of the pulsation of blood vessels near the lesion as well as other movements, e.g. animal gasps due to deep anesthesia. Speckle tracking and subsequent 2D filtering of echo shift data were used to compute estimates of temperature change over every pixel of the M2D frame on an a grid with spacing $18.75 \times 200\mu m^2$ in the axial and lateral dimensions and with a 1/91 sec time step. This fine spatial and temporal resolution allowed for the computation of both temporal and spatial derivatives without noise amplification. For example, the initial heating rate (IHR) was computed over every pixel of the M2D frame as a function of time. In conjunction with subtherapeutic FUS beams, peak of the IHR

occurred approximately at the focal location with values depending on the intensity of the beam and local absorption.

6.2.5 Image Registration

Three-step Registration Based on 3D US/MRI Images

The quality of real-time US imaging was too poor to allow for reliable registration of gross histology and led to unsatisfactory results (using CPD and other methods). This was primarily due to the difficulty of identifying landmarks on the US images to guide the deformation procedure. However, it is well known that 3D US, especially in C-mode, provides significantly improved feature detection. Furthermore, the superior soft tissue contrast provided by 3D MRI can help further refine the feature detection process. This 3-step registration process combined 3D data from both modalities as depicted in Figure 6.4.

The first step involved the alignment of two fixed tissue volumes using 3D US and 3D MRI. The US volume was normalized to match the voxel dimensions of the MRI volume. Next the upper surface boundary of the rat leg was extracted from both the MRI and US fixed volumes. The registration was done using the CPD algorithm, described in [50]. Approximately 4000 points were extracted from both volumes, and because of these large point sets the fast Gauss transform was used during the registration. The alignment between US and MRI volumes was assumed to be affine due to the fixed nature of the tissue. The final volume correspondence was examined, and any additional volume transformations were done manually.

The second step involved manual localization of the 2D gross cross-section within the MRI volume (slice to volume registration). This was performed manually using clear features, e.g. bone, connective tissue and fat. This step resulted in an MRI-equivalent of the gross cross section.

The third step relied on steps 1 and 2, which revealed landmarks seen both on the real-time US and the gross cross-section. During this step the *in vivo* US image was aligned with the gross image based on a nonrigid point set registration.

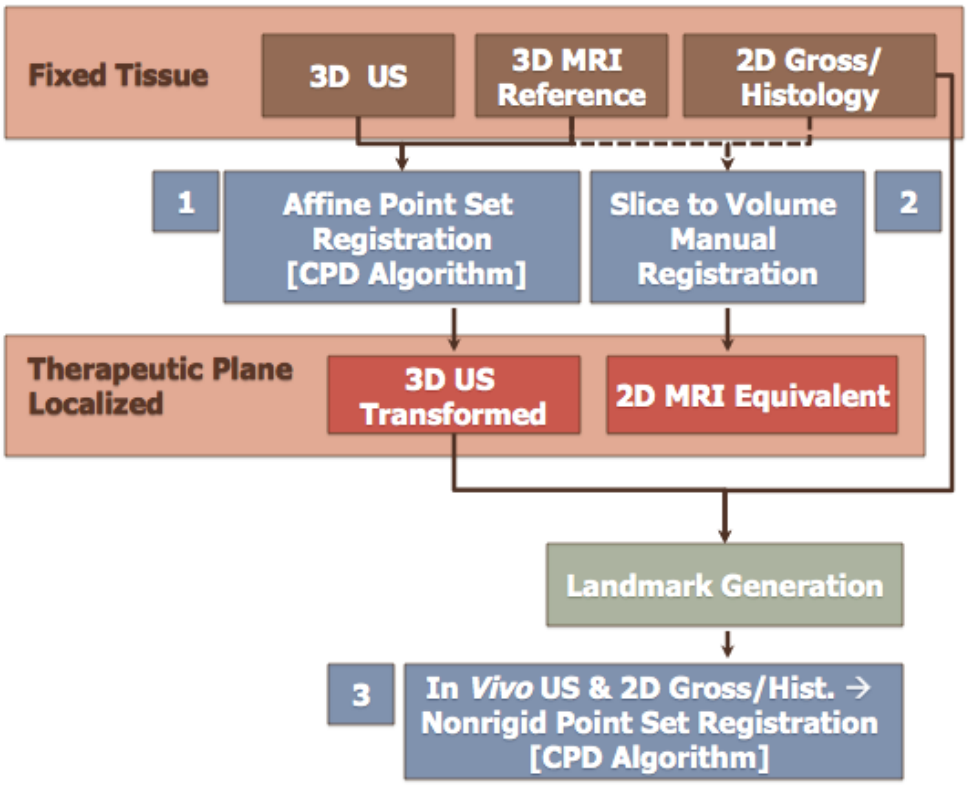

Figure 6.4: A flow diagram of the image registration algorithm.

CPD Algorithm Summary

The CPD algorithm described in [50] provided a robust registration tool for both 3D and 2D data sets and gave considerable insight which was key, especially given the nature of US imaging. In this algorithm, the matching of two point sets was modeled as a probability density estimation problem. The first point set, the Gaussian Mixture Model (GMM) centroids, was aligned with the second point set, also known as the data points. This alignment was done through the expectation maximization (EM) algorithm. The key feature of this algorithm is the motion coherence constraint, which, when imposed onto the velocity field, preserves the topological orientation of the point sets. For our problem, we found the CPD to be quite useful in both the 3D US-MRI registration and the 2D US-Gross registration. The algorithm was largely the same for both cases, except for the use of the transformation operator, which was affine for the 3D case and nonrigid for the 2D case. Reference [50] provides an excellent description of the algorithm for the interested reader.

6.3 Results and Discussion

The results of lesion formation in tissue Block # 1 are summarized in Figure 6.2a, where five volumetric lesions (L1-L5) are seen with each lesion comprising five individual foci. In Figure 6.2b and 6.2b1 gross lesions within Block # 2 are captured, and labeled L1 through L8. During gross inspection the volumetric lesions in Block # 2 appear more homogeneous. It is hypothesized that decreasing inter-foci spacing from 0.55mm to 0.50 mm sustained the more coherent temperature distribution needed for a continuous volumetric lesion.

Once lesions were localized and inspected, the axial-temporal profile for each lesion was analyzed. Figure 6.3 illustrates spatial-temporal temperature maps at 760 W/cm^2 intensity before (a) and after (b) lesion formation. Individual traces for five acoustic intensities are seen in Figure 6.3c. Pronounced temperature increases and heating rates were observed after therapy for the majority of lesions in Block # 1. Also, close

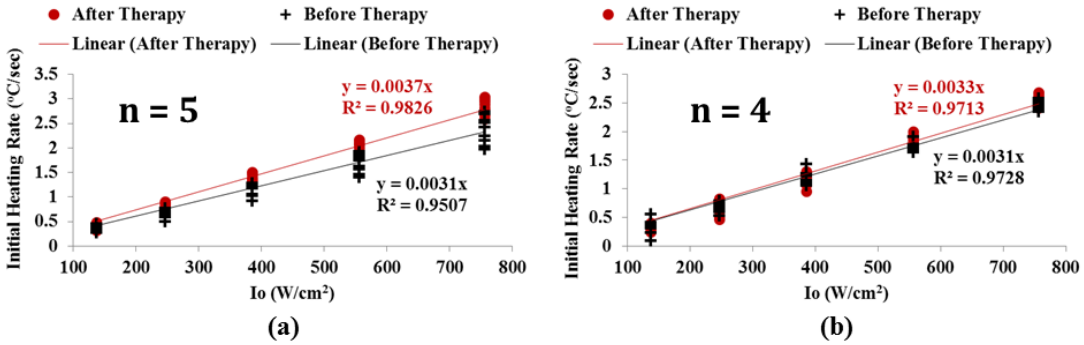

Figure 6.5: Statistics summary for (a) tissue Block # 1 for locations L1 through L5, and (b) tissue Block # 2 for locations L1, L6, L7 and L8.

Table 6.1: Summary of Initial Heating Rates Pre and Post Therapeutic Lesion Formation.

	$I_o(W/cm^2)$	H	p	Median (PRE)	Median (POST)	Difference
	140	0	0.21360	0.38	0.41	10%
Tissue	250	1	0.00054	0.70	0.84	20%
Block #1	390	1	0.00001	1.18	1.35	15%
	560	1	0.00002	1.75	2.07	18%
	760	1	0.00002	2.46	2.84	16%
	$I_o(W/cm^2)$	H	p	Median (PRE)	Median (POST)	Difference
	140	0	0.96000	0.34	0.34	2%
Tissue	250	0	0.92330	0.67	0.67	0%
Block #2	390	0	0.70420	1.14	1.23	7%
	560	1	0.00540	1.67	1.87	11%
	760	1	0.04510	2.46	2.58	5%

agreement between the temperature profiles acquired during subtherapeutic shots delivered prior to therapy in increasing intensities and decreasing intensities, established the repeatability of the measurement. This ensured that the tissue was not thermally modified as a result of the measurement.

The initial heating rate measurements for all subtherapeutic shots before and after therapy delivery are summarized in scatter plots in Figures 6.5a and b. A statistical summary of these measurements appears in Table 6.1. As seen from the table, the null hypothesis was supported for the lowest exposure (140 W/cm^2). However, for the remainder of the subtherapeutic exposure groups the null hypothesis was rejected with $p \leq 0.01$.

In tissue Block # 2, a strong degree of change in the initial heating rate was observed at locations L2, L3, and L5. The lesions formed at locations L1, L6, L7, and L8 exhibited only a small change in the initial heating rate. These four lesions are depicted on the graph in Figure 6.5b. When performing the Student's t-test for each subtherapeutic exposure group before and after therapy, no pronounced difference was observed for the three lowest exposures (140 W/cm^2, 250 W/cm^2, 390 W/cm^2). The highest two exposures, 560 W/cm^2 ($p \leq 0.01$) and 760 W/cm^2 ($p \leq 0.05$), exhibited a pronounced difference in the heating rate before and after therapy. Also, upon gross examination these four locations corresponded to lesions lighter in color than the lesions at locations L2 and L3 (L5 was excluded from comparison due to the presence of connective tissue).

In addition to a documented increase in the heating rate for the post therapy measurements, a higher temperature rise following therapy was observed spatially on an axial-temporal slice for all block # 1 lesions and block # 2 lesions L2, L3, and L5.

6.3.1 Noninvasive IgFUS *In Vivo* Small-animal Model

Figure 6.6 shows a representative cross-section through the rat thigh, where 6.6(a) is the reference MRI volume, 6.6(b) is the unregistered US volume and 6.6(c) is the 3D ultrasound volume that was registered with the affine CPD algorithm. On the ultrasound cross-section, specular structures can be visualized surrounding the boundary of the rat

leg. These are bubbles of air trapped within unshaven skin regions. From the images we can also identify a connective tissue triangle, appearing black on the right side of the MRI cross-section. This same triangle appears hyperechoic on the US image.

After taking these images, we localized the therapeutic plane within the 3D MRI volume. In Figure 6.7(a) the representative cross-section through the therapeutic plane is seen, with both formed HIFU lesions outlined by white rectangles. The gross image seen in Figure 6.7(a) was used as a sliding reference to identify the corresponding treatment plane within the MRI volume. For localization, unique traits were identified, including: two bones (tibia and fibula), a connective tissue triangle with a blood vessel running through it, and visible separation boundaries between different muscles. With the help of these traits, the corresponding MRI cross-section was identified (Figure 6.7(b)), and the bones and skin periphery were outlined by a blue line.

The presence of a therapeutic cross-section in two different modalities (MRI and US) in addition to a gross image allowed us to identify control points to register the *in vivo* US B-mode image with the gross image. Within the *in vivo* ultrasound image seen in Figure 6.8(a) the control points used for the registration are outlined. They include the skin periphery and connective tissue layers that were confirmed through the alignment of 3D MRI and 3D US volumes. Additional control points were extracted from the strain data representing microvessels with a diameter between 60 and 100 μm as seen on the histology slides. After the manual placement of control points was complete, they were fed into the nonrigid CPD algorithm. Final alignment of the MRI and ultrasound volumes is seen in Figure 6.8(c), where the blue points are the transformed point set and the red points are the reference point set. The acquired transformation matrix was then applied onto the 2D gross image, with the resultant transformation seen in Figure 6.8(d).

The final step of the process was to overlay the tissue parameters extracted from the M2D onto the registered gross image. Since the M2D window was inherently aligned with the *in vivo* US B-mode image, no additional deformations were needed to register the gross image with the M2D image. The overlay of the heating rate extracted from the ultrasound temperature data before lesion formation is visualized overlaying the gross image in Figure 6.9(b) and after lesion formation in Figure 6.9(c). The results clearly

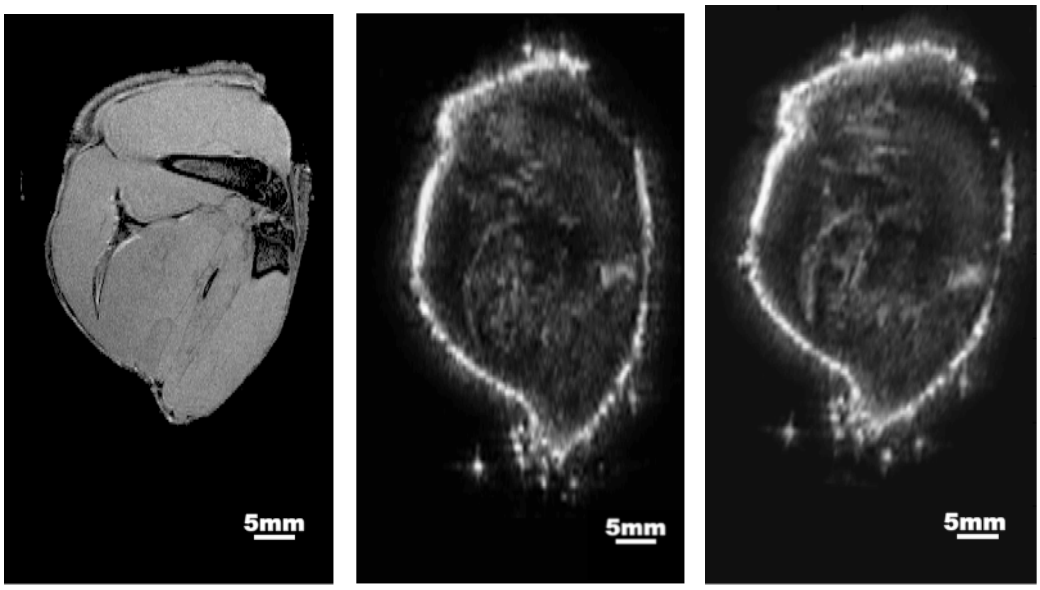

(a) Reference MRI (b) Initial US (c) Aligned US

Figure 6.6: Representative cross-sections from 3D MRI/US data.

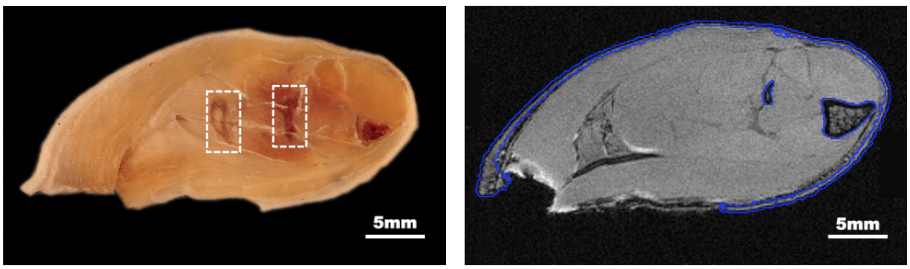

(a) Gross Image (b) MRI Cross-section

Figure 6.7: Therapeutic plane cross-section visualized on registered MRI and gross image cross-sections. White boxes outline two lesions formed at the time of therapy.

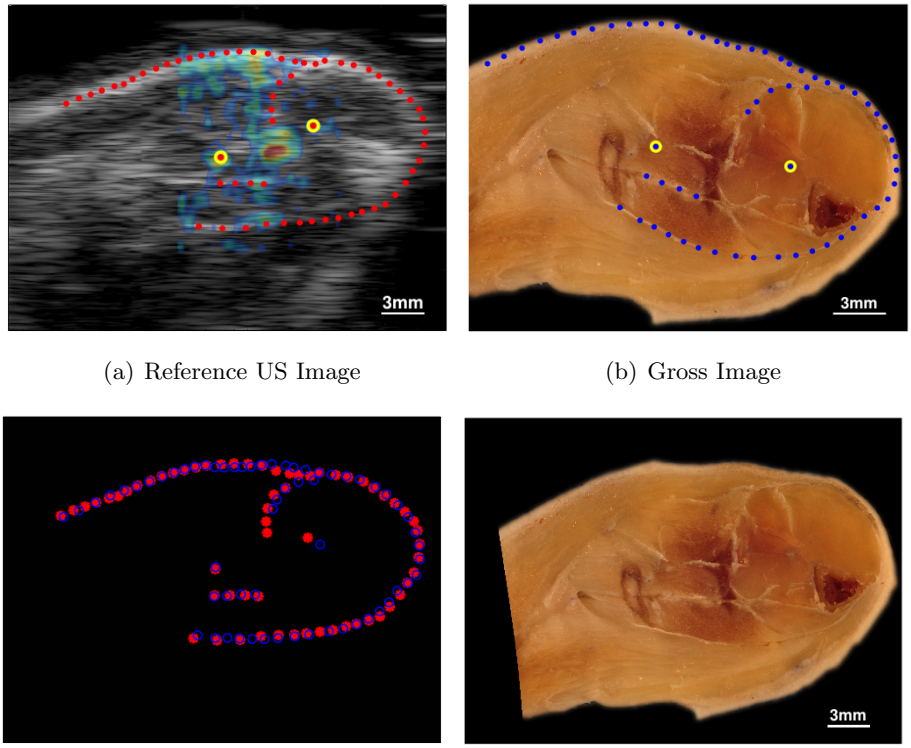

(a) Reference US Image

(b) Gross Image

(c) Point Sets Aligned

(d) Transformed Image

Figure 6.8: *In vivo* US image (a) with the corresponding control points depicted in red, to be co-registered with the gross image depicted in (b). For (a) and (b) yellow circles represent control points associated with the microvessels. The result of the registered points sets through Nonrigid CPD algorithm is depicted in (c), the corresponding transformed image (d).

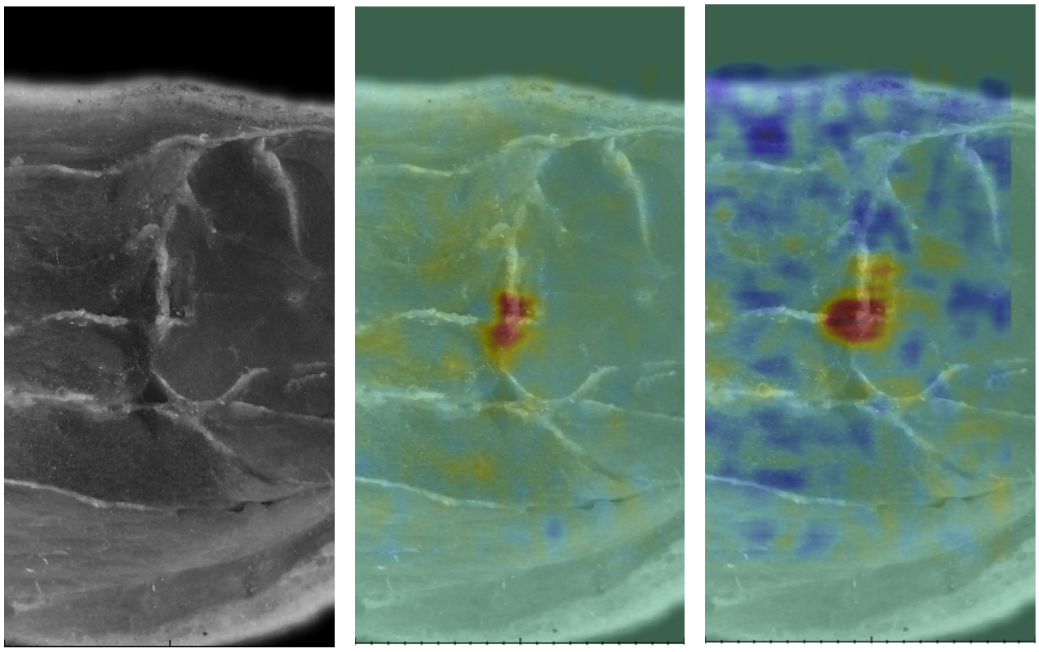

(a) Gross Image (b) Pre-therapy (c) Post-therapy

Figure 6.9: Heating rate projected onto the gross image (a), before (b) and after (c) therapy.

show: 1) the correspondence between the high IHR and the target lesion location, and 2) the increase in size of the IHR after lesion formation, indicating a change in absorption.

Even in the small animal rodent model used to obtain the results presented in this chapter, it is seen that motion and tissue deformations are significant enough to call for correction using robust registration algorithms. Our initial effort to associate subsurface landmarks from the real-time 2D ultrasound with anatomical features on gross histology produced mixed results. The incorporation of 3D imaging data, both MRI and US, allowed for reliable landmark identification with improved localization.

The quality of the real-time ultrasound imaging used in these experiments was compromised to some extent by the water coupling which increased reverberations and reduced contrast. Despite these limitations, the quality of the registration allowed for the mapping of the UST-based quantitative (spatial) measurements onto the actual lesion location.

6.4 Conclusion

We have shown that subtherapeutic shot delivery combined with DMUA imaging, enabled estimation of a localized heating rate indicative of tissue damage. Real-time guidance and the monitoring of therapeutic HIFU beams with DMUA, make ultrasound thermography a powerful tool that will help FUS surgery reach its potential as a safe and effective noninvasive treatment for a variety of diseases.

Chapter 7

Conclusions and Future Work

The work presented in this thesis focused on the use of ultrasound thermography as an image-guidance approach to visualize FUS-tissue (thermal) interactions. This evaluation was performed using two systems, 1) DMUA only and 2) DMUA integrated with a diagnostic ultrasound scanner. Both systems successfully demonstrated the advantages of using thermography in conjunction with the subtherapeutic FUS delivery. These advantages include localization of the beam, treatment planning and damage assessment following lesion formation.

In Chapters 3 and 4, we demonstrated the feasibility of real-time image-guided placement and monitoring of transcranial focused ultrasound (tFUS) beams using DMUAs in a rat model. Synthetic aperture (SA) DMUA imaging was shown to reliably capture key anatomical features delineating the scalp, the skull and the base of the skull. Furthermore, pulsating arteries within the imaging field of view are often detectable on SA imaging. This is significant since vessels are often the target of potential transcranial therapies. We have also demonstrated that real-time transcranial ultrasound thermography *in vivo* is capable of detecting and localizing the subtherapeutic transcranial FUS heating profile with high spatial and temporal resolution. The heating rates estimated *in vivo* were consistent with those measured *ex vivo* using thermocouples during the application of subtherapeutic tFUS patterns with similar acoustic power outputs. Some

artifacts were observed on spatio-temporal temperature change profiles, but they neither obscured the actual heating pattern, nor limited our ability to localize the tissue response to tFUS.

A thorough characterization of DMUA imaging and therapy through the skull was performed in Chapter 5. Mapping the DMUA field with a hydrophone allowed the confirmation of a localized profile of the DMUA focus through the mid-section of skull at 3.2 MHz. Furthermore, an insertion loss study revealed both spatial and frequency dependence of the energy loss through the skull. These preliminary findings are likely to be further strengthened by the application of planned adaptive refocusing for improved transcranial imaging and therapy with DMUAs. Not only will the DMUA approach provide a means to guide the placement of tFUS beams, but it will also provide highly specific imaging characterizing the tFUS-tissue interactions. This could be the key to a better understanding of the mechanisms at play in major applications like neuromodulation, the blood-brain barrier opening, and an enhanced delivery of therapeutic agents.

In Chapter 6, we propose a subtherapeutic shot delivery protocol to measure changes in tissue properties due to HIFU lesion formation both *ex vivo* and *in vivo*. This protocol was validated both through gross tissue and histological examination. The heating rate measurements taken *ex vivo* revealed that sub-therapeutic imaging could be used as a quantitative tool for tissue damage assessment. Furthermore, *in vivo* results conducted in the hind limb of a rat further were in line with the *ex vivo* findings.

Focused ultrasound is becoming more widely accepted in the clinic in a variety of applications. However, there is still an urgent need for more quantitative guidance method with high specificity to FUS-tissue interactions. The ability to register real-time US to the histology/gross pathology is an important step towards the validation of tissue property measurements based on ultrasound thermometry. The measured tissue parameters can be directly correlated to different zones of damage seen on histology. This is a key step towards the use of ultrasound thermography data as a tool to predict and quantify tissue damage after HIFU treatment. The ability to analyze and potentially predict different types of damage based on the temperature maps will enable physicians to target specific tissues with a high degree of confidence. The high temporal and spatial

resolution of ultrasound thermography has the potential to improve both the safety and efficacy of noninvasive ultrasound guided HIFU.

Bibliography

[1] Fry W.J. and Barnard J.W., "Selective action of ultrasound on nerve tissue," 1954 IRE Convention Record, pt. 6, pp. 102-106.

[2] Fry W.J. "Ultrasound in neurology." Neurology 6.10 (1956): 693-693.

[3] Fry F.J., "Precision high intensity focusing ultrasonic machines for surgery." American Journal of Physical Medicine & Rehabilitation 37.3 (1958): 152-156.

[4] Fry W.J, Fry F.J., "Fundamental neurological research and human neurosurgery using intense ultrasound." IRE Trans Med Electron. 1960 Jul;ME-7:166-81.

[5] Fry, W.J. "Intense ultrasound in investigations of the central nervous system." Adv Biol Med Phys 6 (1958): 281-348.

[6] Fry F.J., "Production of reversible changes in the central nervous system by ultrasound," Abstr. Natl. Biophys. Conf., Columbus, Ohio, pp. 30-31; 1957.

[7] Fry F.J., Ades H.W., Fry W.J., "Production of reversible changes in the central nervous system by ultrasound." Science. 1958 Jan 10;127(3289):83-4.

[8] Barnard J.W., Fry W.J., Fry F.J., Brennan J.F., "Small localized ultrasonic lesions in the white and gray matter of the cat brain." AMA Arch Neurol Psychiatry. 1956 Jan;75(1):15-35.

[9] Haar G.T., Coussios C., "High intensity focused ultrasound: physical principles and devices." Int J Hyperthermia. 2007 Mar;23(2):89-104. Review.

[10] Lele P.P., "Effect of Ultrasound on solid mammalian tissues and tumors in vivo." In: Repacholi MGH, Randi M, Ed A, eds. Ultrasound: Medical Applications, Biological Effects and Hazard Potential. New York: Plenum, 1987.

[11] Lele P.P. and Pierce A.D., "The thermal hypothesis of the mechanism of ultrasonic focal destruction in organized tissues", in: "Interactions of ultrasound and biological tissues - workshop proceedings", p.121, Reid J. M. and Sikov M. R., eds., U.S.D.H.E.W. Publication (FDA) 73-8008 BRH/DBE 73-1 (1972).

[12] Holt R.G., Roy R.A., "Measurements of bubble-enhanced heating from focused, MHz-frequency ultrasound in a tissue-mimicking material." Ultrasound Med Biol. 2001 Oct;27(10):1399-412.

[13] Rivens I., Shaw A., Civale J., Morris H., "Treatment monitoring and thermometry for therapeutic focused ultrasound." Int J Hyperthermia. 2007 Mar;23(2):121-39.

[14] Bohris C., Schreiber W.G., Jenne J., Simiantonakis I., Rastert R., Zabel H.J., Huber P., Bader R., Brix G., "Quantitative MR temperature monitoring of high-intensity focused ultrasound therapy." Magn Reson Imaging. 1999 May;17(4):603-10.

[15] Wu T., Felmlee J.P., Greenleaf J.F., Riederer S.J., Ehman R.L., "MR imaging of shear waves generated by focused ultrasound." Magn Reson Med. 2000 Jan;43(1):111-5.

[16] Salomir R., Delemazure A.S., Palussire J., Rouvire O., Cotton F., Chapelon J.Y., "Image-based control of the magnetic resonance imaging-guided focused ultrasound thermotherapy." Top Magn Reson Imaging. 2006 Jun;17(3):139-51. Review.

[17] Illing R.O., Kennedy J.E., Wu F., ter Haar G.R., Protheroe A.S., Friend P.J., Gleeson F.V., Cranston D.W., Phillips R.R., Middleton M.R., "The safety and feasibility of extracorporeal high-intensity focused ultrasound (HIFU) for the treatment of liver and kidney tumours in a Western population." Br J Cancer. 2005 Oct 17;93(8):890-5.

[18] Wu F., ter Haar G., Chen W.R., "High-intensity focused ultrasound ablation of breast cancer." Expert Rev Anticancer Ther. 2007 Jun;7(6):823-31. Review.

[19] Seip R., Ebbini E.S., O'Donnell M., Cain C.A., "Non-invasive detection of thermal effects due to highly focused ultrasonic fields," Ultrasonics Symposium, 1993. Proceedings., IEEE 1993 , vol., no., pp.1229,1232 vol.2, 31 Oct-3 Nov 1993

[20] Seip R., Ebbini E.S., "Noninvasive estimation of tissue temperature response to heating fields using diagnostic ultrasound." IEEE Trans Biomed Eng. 1995 Aug;42(8):828-39.

[21] Maass-Moreno R., Damianou C.A., "Noninvasive temperature estimation in tissue via ultrasound echo-shifts. Part I. Analytical model." J Acoust Soc Am. 1996 Oct;100(4 Pt 1):2514-21.

[22] Maass-Moreno R., Damianou C.A., Sanghvi N.T., "Noninvasive temperature estimation in tissue via ultrasound echo-shifts. Part II. In vitro study." J Acoust Soc Am. 1996 Oct;100(4 Pt 1):2522-30.

[23] Simon C., Vanbaren P., Ebbini E.S. "Two-dimensional temperature estimation using diagnostic ultrasound." IEEE Trans Ultrason Ferroelectr Freq Control. 1998;45(4):1088-99.

[24] Ophir J., Cspedes I., Ponnekanti H., Yazdi Y., Li X., "Elastography: a quantitative method for imaging the elasticity of biological tissues. Ultrason Imaging." 1991 Apr;13(2):111-34.

[25] Righetti R., Kallel F., Stafford R.J., Price R.E., Krouskop T.A., Hazle J.D., Ophir J., "Elastographic characterization of HIFU-induced lesions in canine livers." Ultrasound Med Biol. 1999 Sep;25(7):1099-113.

[26] Kallel F., Stafford R.J., Price R.E., Righetti R., Ophir J., Hazle J.D., "The feasibility of elastographic visualization of HIFU-induced thermal lesions in soft tissues. Image-guided high-intensity focused ultrasound." Ultrasound Med Biol. 1999 May;25(4):641-7.

[27] Souchon R., Soualmi L., Bertrand M., Chapelon J.Y., Kallel F., Ophir J., "Ultrasonic elastography using sector scan imaging and a radial compression." Ultrasonics. 2002 May;40(1-8):867-71.

[28] Souchon R., Rouvire O., Gelet A., Detti V., Srinivasan S., Ophir J., Chapelon J.Y., "Visualisation of HIFU lesions using elastography of the human prostate in vivo: preliminary results." Ultrasound in medicine & biology 29.7 (2003): 1007-1015.

[29] Fatemi M., and Greenleaf J.F., "Vibro-acoustography: An imaging modality based on ultrasound-stimulated acoustic emission." Proceedings of the National Academy of Sciences 96.12 (1999): 6603-6608.

[30] Farny C.H., Glynn Holt R., Roy R.A., "The correlation between bubble-enhanced HIFU heating and cavitation power." IEEE Trans Biomed Eng. 2010 Jan;57(1):175-84.

[31] Gyongy M., and Coussios C-C., "Passive spatial mapping of inertial cavitation during HIFU exposure." Biomedical Engineering, IEEE Transactions on 57.1 (2010): 48-56.

[32] Park M.J., Kim Y.S., Keserci B., Rhim H., Lim H.K., "Volumetric MR-guided high-intensity focused ultrasound ablation of uterine fibroids: treatment speed and factors influencing speed." Eur Radiol. 2013 Apr;23(4):943-50.

[33] Ebbini E.S., Yao H., Shrestha A., "Dual-mode ultrasound phased arrays for image-guided surgery." Ultrason Imaging. 2006 Apr;28(2):65-82.

[34] Wan Y., Ebbini E.S., "Imaging with concave large-aperture therapeutic ultrasound arrays using conventional synthetic-aperture beamforming." IEEE Trans Ultrason Ferroelectr Freq Control. 2008 Aug;55(8):1705-18.

[35] Chapelon J.Y., Cathignol D., Cain C., Ebbini E., Kluiwstra J.U., Sapozhnikov O.A., Fleury G., Berriet R., Chupin L., Guey J.L., "New piezoelectric transducers for therapeutic ultrasound." Ultrasound Med Biol. 2000 Jan;26(1):153-9.

[36] Casper A.J., Liu D., Ballard J.R., Ebbini E.S., "Real-time implementation of a dual-mode ultrasound array system: *in vivo* results." IEEE Trans Biomed Eng. 2013 Oct;60(10):2751-9.

[37] Bayat M., Ballard J.R., Ebbini E.S., "Adaptive motion compensation for *in vivo* ultrasound temperature estimation," Ultrasonics Symposium (IUS), 2013 IEEE International , vol., no., pp.1797,1800, 21-25 July 2013

[38] Liu D., Haritonova A., Ebbini E., "Close-loop lesion formation control using multiple-focus dual mode ultrasound array," Ultrasonics Symposium (IUS), 2014 IEEE International , vol., no., pp.1634,1637, 3-6 Sept. 2014

[39] Yao H., and Ebbini E.S., "Refocusing dual-mode ultrasound arrays in the presence of strongly scattering obstacles," Ultrasonics Symposium, 2004 IEEE , vol.1, no., pp.239,242 Vol.1, 23-27 Aug. 2004

[40] Ballard J.R., Casper A.J., Wan Y., Ebbini E.S., "Adaptive transthoracic refocusing of dual-mode ultrasound arrays." IEEE Trans Biomed Eng. 2010 Jan;57(1):93-102.

[41] Poguet J., Dumas P., Fleury G.,"Piezocomposite technology : An innovative approach to the improvement of N.D.T. performance using ultrasounds", 8th European Conference on Non Destructive Testing, June 2002, Barcelona, Spain.

[42] Liu D., Ebbini E.S., "Real-time 2-D temperature imaging using ultrasound." IEEE Trans Biomed Eng. 2010 Jan;57(1):12-6. doi: 10.1109/TBME.2009.2035103. Epub 2009 Oct 30.

[43] Seip R., VanBaren P., Cain C.A., Ebbini E.S., "Noninvasive real-time multipoint temperature control for ultrasound phased array treatments." Ultrasonics, Ferroelectrics, and Frequency Control, IEEE Transactions on 43.6 (1996): 1063-1073.

[44] Maass-Moreno R., Damianou C.A., Sanghvi N.T., "Tissue temperature estimation in-vivo with pulse-echo," Ultrasonics Symposium, 1995. Proceedings., 1995 IEEE , vol.2, no., pp.1225,1229 vol.2, 7-10 Nov 1995

[45] Seip R., "Feedback for ultrasound thermotherapy." University of Michigan, 1996.

[46] Nasoni R., and Bowen T., "Ultrasonic speed as a parameter for noninvasive thermometry." Non-invasive temperature measurement 1 (1989): 95-107.

[47] Frizzell L.A., "Threshold dosages for damage to mammalian liver by high intensity focused ultrasound." IEEE Trans Ultrason Ferroelectr Freq Control. 1988;35(5):578-81.

[48] Fry F.J., and Barger J.E., "Acoustical properties of the human skull." J Acoust Soc Am. 1978 May;63(5):1576-90.

[49] Parker K.J. and Lele P.P., "The Thermal Pulse-Decay Method for Determining Ultrasound Absorption Coefficients," *1982 Ultrasonics Symposium*, 754 (1982).

[50] Myronenko A., and Song X., "Point set registration: Coherent point drift." Pattern Analysis and Machine Intelligence, IEEE Transactions on 32(12), pp. 2262-2275. 2010.

Appendix A

DMUA Characterization

A.1 DMUA Power Charcaterization

A.1.1 Methods

To estimate the power output of the DMUA, ultrasound power was measured with an Ultrasound Power Meter (Model UPM-DT 100AV, Ohmic Instruments Inc., Easton, MD, USA). The power meter was filled with degassed deionized water (24°C) and positioned under a motorized stage to which a 3.5 MHz DMUA was secured (as seen in Figure A.1). The array was first cleaned with an antiseptic alcohol wipe towelette and then encapsulated inside a water bolus, filled with degassed water (24°C). The bolus was incorporated to simulate *in vivo* experimental conditions.

To ensure accurate power measurement, the geometric focal point of the array was aligned with the 45° conical target of the ultrasound power meter. SA imaging provided visual feedback for accurate positioning of the ultrasound transducer and enabled post measurement monitoring for potential disturbances of the cone. On the SA image the cone tip was positioned at 39 mm, allowing the cone to intercept the focal beam of the transducer. Imaging feedback also confirmed a lack of mechanical vibrations in the environment. After the two systems were aligned, the cone of the power balance was calibrated with a 1gr = 14.5 W weight. Next a set of subtherapeutic voltages was

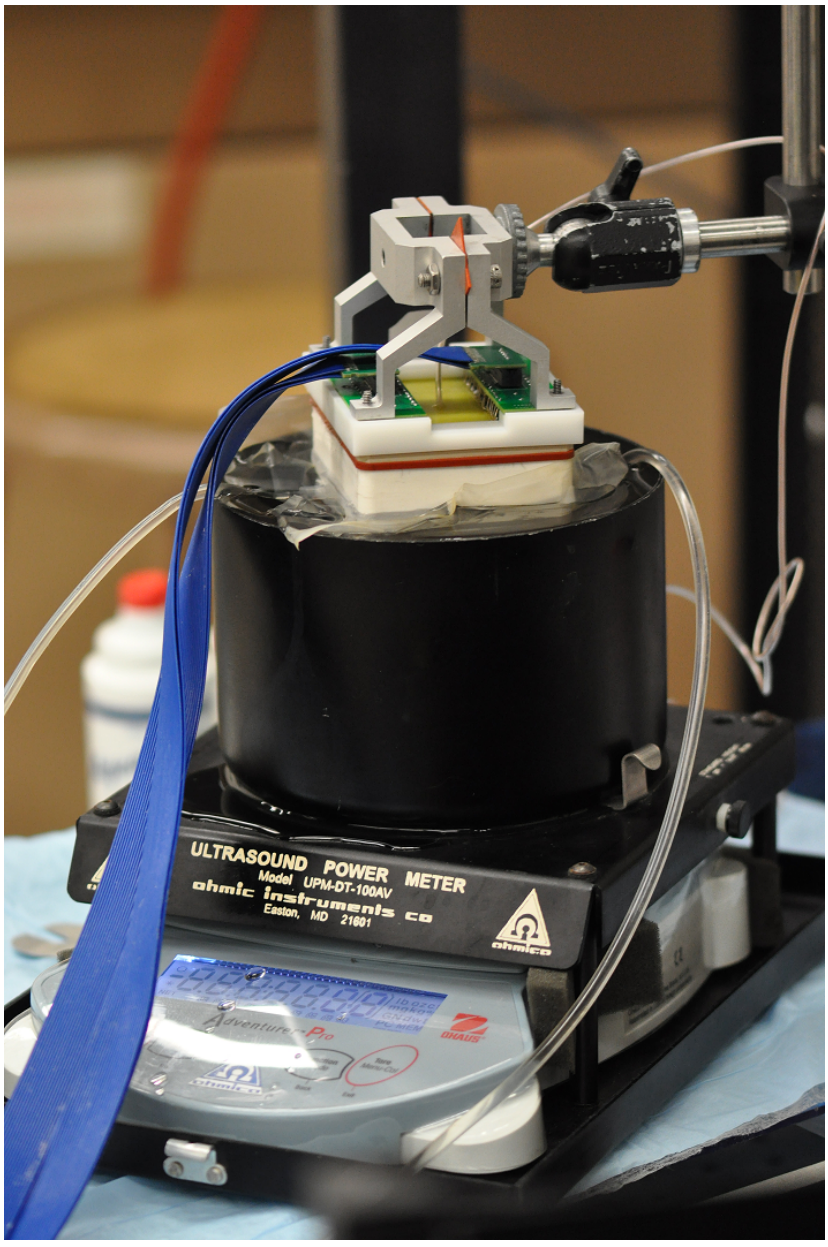

Figure A.1: DMUA positioned for ultrasonuic power measurement. The ultrasound power meter used for the measurement was manufactured by Ohmic Instruments Co. (Model UPM-DT-100AV, Easton, MD, USA)

calibrated, from 50 mV to 425 mV, with a step size of 25 mV. For each voltage the DMUA delivered power for a period of 3sec and the measurement was repeated three times.

Results

Figure A.2 summarizes the power measured for voltages between 50 mV and 425 mV. The numerical averages of the power levels over the three trials were also listed in Table A.1 and A.2. A linear relationship between squared voltages and the power was observed up until 425 mV; the equation $y = 10^{-5}x$ was obtained by fitting points between 50 mV and 300 mV and setting the intercept to zero. This equation allows the estimation of intermediate power values for subtherapeutic exposures, assuming a linear dependence for the subtherapeutic exposures.

A.2 DMUA Beam Profile Characterization

A.2.1 Hydrophone Scans

Methods

The measurement of the pressure field for a fenestrated DMUA transducer was collected with the 0.2mm Onda hydrophone. The hydrophone signal was amplified with a AH-2010 preamplifier, and transmitted through a coaxial cable to the Tektronix oscilloscope (model TDS5104B, Beaverton, OR, USA). To acquire a spatial pressure map, the DMUA transmitted a 10 μs pulse at 3.2MHz each time a 3-axis stage motor (Quicksilver Controls Inc., Covina, CA, USA) moved to a new location. Each transition triggered the scope enabling an accurate capture of the signal.

For each spatial location of the hydrophone a raw trace from the oscilloscope was transferred through a GPIB interface (16-bit DAQ on the Oscilloscope) to the PC and stored. In the axial-lateral scan the spacing was 250μm in axial and lateral dimensions. In the elevation-lateral scan the spacing was 125μm in elevation and lateral dimensions.

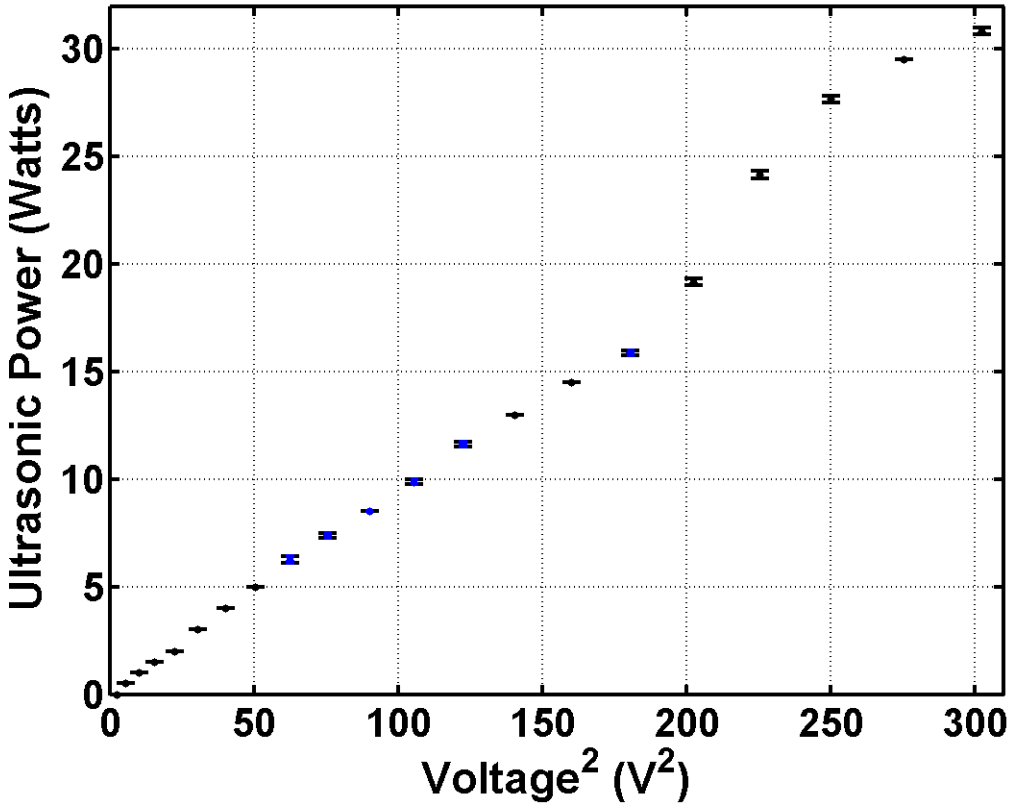

Figure A.2: Ultrasonic power measurements as measured by the power meter for a range of voltages between 50 mV and 550 mV.

Table A.1: Ultrasonic Power Values Summarized for a Range of Subtheraputic Voltages

Voltage (mV)	50	75	100	125	150	175	200	225	250	275
Power (W)	0	0.5	1.0	1.5	2.0	3.0	4.0	5.0	6.3	7.4

Table A.2: Ultrasonic Power Values Summarized for Voltages above 300mV

Voltage (mV)	300	325	350	375	400	425	450	475	500	525	550
Power (W)	8.5	9.9	11.6	13.0	14.5	15.9	19.2	24.2	27.7	29.5	30.8

The intensity maps were constructed in MATLAB (MathWorks, Natick, MA, USA). Each trace was detrended, filtered with a band-pass filter, and the RMS of the sinusoidal signal acquired for each pixel producing a 2D map representative of the pressure profile of the array. Next the intensity was computed by squaring the pressure equivalent and normalizing the maximum to one W/cm^2. The spline interpolation was applied to the final 2D map to achieve 0.041 mm spacing between each pixel.

Results

Figure A.3 depicts the resulting normalized intensity profile for a 3.5MHz DMUA. In the axial-lateral plane (Figure A.3(a)) the focus was asymmetrical due to several dysfunctional array channels. In the lateral-elevation plane (Figure A.3(b)) three pronounced foci are seen at: (0 mm, -1 mm), (0 mm, 0 mm) and (0 mm, +1 mm). The resolution values are summarized in Table A.3.

Table A.3: Beam Resolution for a 3.5MHz Fenestrated DMUA

FWHM	Fenestrated DMUA (S/N 8660, A102)
Axial (mm)	2.440
Lateral (mm)	0.473
Elevation (mm)	0.443

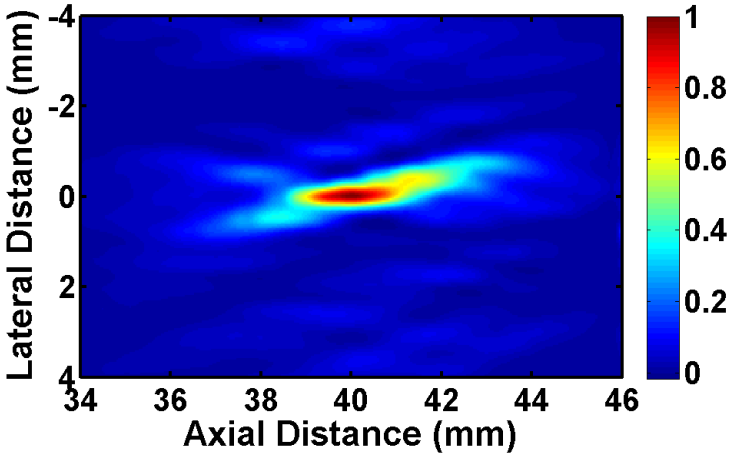

(a) Axial-Lateral Normalized Intensity

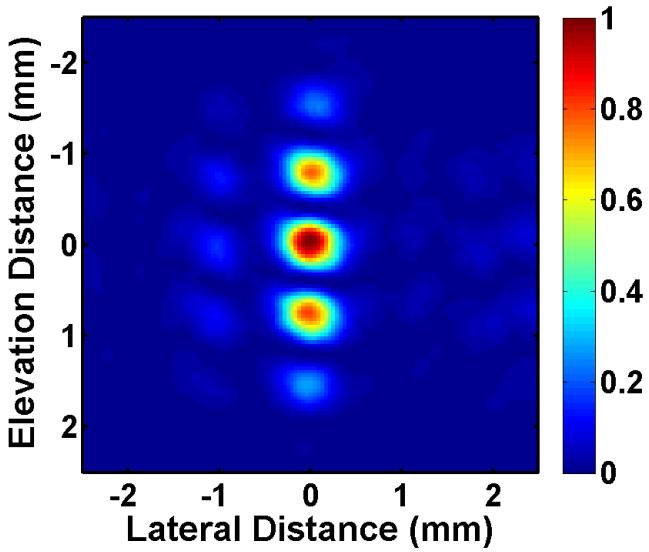

(b) Lateral-Elevation Normalized Intensity

Figure A.3: Hydrophone Scans for 3.5MHz Fenestrated DMUA (S/N 8660, A102)

Appendix B

Acronyms

Table B.1: Acronyms

Acronym	Meaning
DMUA	Dual-Mode Ultrasound Array
FUS	Focused Ultrasound
HIFU	High-Intensity Focused Ultrasound
IHR	Initial Heating Rate
MRIgFUS	Magnetic Resonance Imaging-guided Focused Ultrasound
SA	Synthetic Aperture
STF	Single Transmit Focus
tFUS	Transcranial Focused Ultrasound
USgFUS	Ultrasound-guided Focused Ultrasound